
# Università degli Studi di Trieste

XXXII Ciclo del Dottorato di Ricerca in

Nanotecnologie

PO Friuli Venezia Giulia - Fondo Sociale Europeo 2014/2020

# Exciton Dynamics in Molecular Heterojunctions

Settore Scientifico-Disciplinare: FIS/03

Dottorando
**Roberto Costantini**

Coordinatore
**prof. Alberto Morgante**

Supervisore di Tesi
**prof. Alberto Morgante**

Co-Supervisore
**dr. Albano Cossaro**

Anno Accademico 2018/2019


# Università degli Studi di Trieste

XXXII Ciclo del Dottorato di Ricerca in

Nanotecnologie

PO Friuli Venezia Giulia - Fondo Sociale Europeo 2014/2020

# Exciton Dynamics in Molecular Heterojunctions

Settore Scientifico-Disciplinare: FIS/03

Dottorando

**Roberto Costantini**

Coordinatore

**prof. Alberto Morgante**

Supervisore di Tesi

**prof. Alberto Morgante**

Co-Supervisore

**dr. Albano Cossaro**

---

Anno Accademico 2018/2019

# Abstract

In recent years, the need for a more sustainable economic development contributed to the increasing interest in renewable energy sources. With encouraging trends on power conversion efficiencies and manufacturing costs, photovoltaics is expected to be the workhorse for the production of green energy in the future. Silicon is currently the dominant photovoltaic technology but, in the past decade, novel solutions based on organic semiconductors became attractive for their potential of overcoming the Shockley-Queisser limit and offering unmatched efficiencies by exploiting singlet fission. The latter is an exciton multiplication process in which, for a certain class of materials, a singlet exciton splits into two triplet excitons, thus potentially doubling the charge carriers. Significant work is still necessary to fully benefit of singlet fission in photovoltaics; in particular, a higher degree of control over exciton transport and dissociation mechanisms at hetero-organic interfaces is required for efficiently harvesting triplet excitons. To the aim of better understanding such processes, at the ANCHOR-SUNDYN endstation of the ALOISA beamline at Elettra we developed an experimental setup for time-resolved X-ray spectroscopies, in which the exciton dynamics in organic films can be characterized by X-ray photoemission and absorption spectroscopies with a 100 ps resolution. Here, we can combine time-resolved measurements with standard X-ray and UV spectroscopies for a more detailed analysis of the samples.

We apply this approach to donor/acceptor interfaces, the prototypical architectures of organic photovoltaic devices; we investigate triplet excited states in pentacene by means of time-resolved X-ray absorption, which displays a pump-induced feature with a $0.3 \pm 0.2$ ns lifetime below the LUMO resonance, that we associated to molecules in the triplet state. On the picosecond time scale, measurements performed at the FLASH free-electron laser reveal a photoelectron response that we deem related to the triplet exciton dissociation at the interface with the underlying $C_{60}$ film. A similar effect is also observed in pump-probe photoemission spectra of tetracene / copper phthalocyanine interfaces. On this second system, we tuned the pump wavelength to selectively excite the two materials and examined the different behavior of the photogenerated excitons; the presence of a transient field in the microsecond time scale suggests that triplet excitons are involved in the charge transfer that occurs from tetracene to copper phthalocyanine, in agreement with previous studies. The results presented here demonstrate that time-resolved X-ray spectroscopies can provide valuable information for the characterization of exciton dynamics in hetero-organic interfaces.

# Contents

# 1 Introduction

The growing concern for global warming recently led to a series of climate strikes organized to demand action against climate change, but the need to reduce the $CO_2$ concentration in the atmosphere has been recognized for a long time. This issue was the main topic that was discussed at the 2015 United Nations Climate Change Conference (COP21) in Paris, in which the attending parties agreed to set a 40 - 70% cut of greenhouse gas emission before 2050. This target will require more and more effort as the forecasted growth in both population and economies are likely to cause a 70% increase in the global energy consumption by 2050[1], therefore it is crucial to gradually reduce the use of fossil fuels and veer towards renewable energy sources. With the drop in manufacturing cost and increasing device efficiencies, photovoltaics is expected to hold a 35% share of the additional electricity generation capacity that will be installed by 2040, with silicon still being the dominant technology[2]. Despite the steady improvement in the power conversion efficiencies, which is currently in the range of 21-23% for commercially available cells[3–5], single junction devices have a maximum obtainable efficiency of 32%, knows as the Shockley-Queisser limit[6]. Novel technologies based on organic materials started emerging in the past decade, mainly because their ease of processing, low manufacturing costs and the potential to overcome such efficiency limit[7]. Research aimed specifically at improving the efficiency of organic-based devices above the Shockley-Queisser limit is still at an early stage, but some prototypal devices have already demonstrated effective exciton multiplication for tetracene[8] and pentacene[9] based cells. Exciton multiplication in these materials is obtained through singlet fission, a photophysical process in which the absorption of an optical photon creates a high energy (singlet) exciton that eventually splits into two low energy (triplet) excitons. This mul-

tiplication of charge carriers offers a promising route to increased photocurrent generation. However, even considering the potential gains, the organic technology is far from being able to replace the well-established silicon devices, as the latter have set high standards for quality and durability, which are not currently achievable with organic devices. An intermediate strategy which is also being explored is that of hybrid devices, in which silicon is sensitized with a singlet fission chromophore[10], with the goal of exploiting the exciton multiplication process to mitigate the intrinsic thermalization losses that characterize inorganic semiconductor cells[11]. Still, significant work is necessary to understand and control exciton transport and dissociation mechanisms at hetero-organic interfaces in order to fully benefit of the advantages offered by organic semiconductors and rationally design functional optoelectronic devices.

## 1.1 Aim of the thesis

The main objective of my work was the development and commissioning of an experimental setup for time-resolved X-ray spectroscopies for the characterization of exciton dynamics in organic films. This first task was completed at the ANCHOR-SUNDYN endstation of the ALOISA beamline at the Elettra synchrotron in Trieste. Pump-probe spectroscopies are widely used in the study of electronic dynamics in materials science, but the vast majority of laboratories relies solely on lasers; this means that, due to the low photon energy that is typically available, only a small portion of valence band can be probed. On the other hand, by using X-ray photons as a probe, we can access the core levels and increase the amount of information that can be obtained. Over the past two decades, several setups for time-resolved X-ray spectroscopies have been developed[12–17], but only a few of them are based on electron detectors[18–21]. This is a fundamental requirement for performing X-ray photoemission spectroscopy and a great advantage for detecting X-ray absorption signal in organic materials, due to the higher Auger yield in low-Z atoms. As I will illustrate in Chapter 2, at the ANCHOR-SUNDYN endstation it is now possible to measure both X-ray photoemission and absorption with 100 ps resolution by exploiting the hybrid bunch operation of the Elettra synchrotron[22].
After the successful commissioning, our setup was used for the characterization

of the triplet exciton dynamics in two of the prototypical singlet fission chromophores: pentacene and tetracene. Pentacene is by far the most widely studied molecule for singlet fission, but the experimental studies reported in the literature are usually based on two-photon photoemission[23] or transient optical absorption[24–26] measurements. In Chapter 3, I will report the first evidence of the triplet excited state in X-ray absorption spectra, that was observed with a lifetime of $0.3 \pm 0.2$ ns[27]. Moreover, I will present the time-resolved X-ray photoemission data measured at the FLASH free-electron laser in Hamburg on the pentacene/$C_{60}$/Ag(111) sample, in which we detected a pump-induced shift peaked at $\sim 6$ ps after the optical excitation. As the time scale is comparable to the one reported for the triplet exciton dissociation at the pentacene/$C_{60}$ interface[23,28], we speculate that such shift is induced by a transient electric field related to charge separation.
Finally, on tetracene/copper phthalocyanine interfaces an analogous effect was observed. At the ANCHOR-SUNDYN endstation we combined valence band and two-photon photoemission measurements to determine the energy level alignment of the interface, and predict the direction of a probable exciton transfer and/or dissociation. By changing the deposition sequence, we then observed how the mutual orientation of the two molecular species is altering the ionization energy of valence states, therefore also affecting the energy level alignment. Such analysis was used for interpreting the core level shifts detected in pump-probe X-ray photoemission spectra, as I will show in Chapter 4. In agreement with previous studies[8,29], our results suggest that charge transfer can occur from tetracene to copper phthalocyanine, producing a transient electric field that persists for microseconds.

# References

1. Narbel, P. A.; Hansen, J. P. Estimating the cost of future global energy supply. *Renewable and Sustainable Energy Reviews* **2014**, *34*, 91–97.

2. Green, M. A. Commercial progress and challenges for photovoltaics. *Nature Energy* **2016**, *1*, 1–4.

3. LG neon R. `https://www.lg.com/it/neon-r`.

4. REC n peak. https://www.recgroup.com/en/products/rec-n-peak-en.

5. SunPower X series. https://us.sunpower.com/solar-panels-technology/x-series-solar-panels.

6. Shockley, W.; Queisser, H. J. Detailed balance limit of efficiency of p-n junction solar cells. *Journal of Applied Physics* **1961**, *32*, 510–519.

7. Hanna, M. C.; Nozik, A. J. Solar conversion efficiency of photovoltaic and photoelectrolysis cells with carrier multiplication absorbers. *Journal of Applied Physics* **2006**, *100*, 074510.

8. Jadhav, P. J.; Mohanty, A.; Sussman, J.; Lee, J.; Baldo, M. A. Singlet Exciton Fission in Nanostructured Organic Solar Cells. *Nano Letters* **2011**, *11*, 1495–1498.

9. Congreve, D. N.; Lee, J.; Thompson, N. J.; Hontz, E.; Yost, S. R.; Reusswig, P. D.; Bahlke, M. E.; Reineke, S.; Van Voorhis, T.; Baldo, M. A. External Quantum Efficiency Above 100% in a Singlet-Exciton-Fission-Based Organic Photovoltaic Cell. *Science* **2013**, *340*, 334–337.

10. Einzinger, M.; Wu, T.; Kompalla, J. F.; Smith, H. L.; Perkinson, C. F.; Nienhaus, L.; Wieghold, S.; Congreve, D. N.; Kahn, A.; Bawendi, M. G.; Baldo, M. A. Sensitization of silicon by singlet exciton fission in tetracene. *Nature* **2019**, *571*, 90–94.

11. Hirst, L. C.; Ekins-Daukes, N. J. Fundamental losses in solar cells. *Progress in Photovoltaics: Research and Applications* **2011**, *19*, 286–293.

12. Nilsson, A.; LaRue, J.; Öberg, H.; Ogasawara, H.; Dell'Angela, M.; Beye, M.; Öström, H.; Gladh, J.; Nörskov, J. K.; Wurth, W.; Abild-Pedersen, F.; Pettersson, L. G. Catalysis in real time using X-ray lasers. *Chemical Physics Letters* **2017**, *675*, 145–173.

13. Pietzsch, A.; Föhlisch, A.; Beye, M.; Deppe, M.; Hennies, F.; Nagasono, M.; Suljoti, E.; Wurth, W.; Gahl, C.; Döbrich, K.; Melnikov, A. Towards time resolved core level photoelectron spectroscopy with femtosecond x-ray free-electron lasers. *New Journal of Physics* **2008**, *10*, 033004.

14. Hellmann, S.; Sohrt, C.; Beye, M.; Rohwer, T.; Sorgenfrei, F.; Marczynski-Bühlow, M.; Kalläne, M.; Redlin, H.; Hennies, F.; Bauer, M.; Föhlisch, A.; Kipp, L.; Wurth, W.; Rossnagel, K. Time-resolved x-ray photoelectron spectroscopy at FLASH. *New Journal of Physics* **2012**, *14*, 013062.

15. Bhattacherjee, A.; Pemmaraju, C. D.; Schnorr, K.; Attar, A. R.; Leone, S. R. Ultrafast Intersystem Crossing in Acetylacetone via Femtosecond X-ray Transient Absorption at the Carbon K-Edge. *Journal of the American Chemical Society* **2017**, *139*, 16576–16583.

16. Stebel, L.; Malvestuto, M.; Capogrosso, V.; Sigalotti, P.; Ressel, B.; Bondino, F.; Magnano, E.; Cautero, G.; Parmigiani, F. Time-resolved soft x-ray absorption setup using multibunch operation modes at synchrotrons. *Review of Scientific Instruments* **2011**, *82*, 123109.

17. Zhang, K.; Lin, M. F.; Ryland, E. S.; Verkamp, M. A.; Benke, K.; De Groot, F. M.; Girolami, G. S.; Vura-Weis, J. Shrinking the Synchrotron: Tabletop Extreme Ultraviolet Absorption of Transition-Metal Complexes. *Journal of Physical Chemistry Letters* **2016**, *7*, 3383–3387.

18. Giangrisostomi, E.; Ovsyannikov, R.; Sorgenfrei, F.; Zhang, T.; Lindblad, A.; Sassa, Y.; Cappel, U. B.; Leitner, T.; Mitzner, R.; Svensson, S.; Mårtensson, N.; Föhlisch, A. Low Dose Photoelectron Spectroscopy at BESSY II: Electronic structure of matter in its native state. *Journal of Electron Spectroscopy and Related Phenomena* **2018**, *224*, 68–78.

19. Silly, M. G. et al. Pump−probe experiments at the TEMPO beamline using the low-$\alpha$ operation mode of Synchrotron SOLEIL. *Journal of Synchrotron Radiation* **2017**, *24*, 886–897.

20. Yamamoto, S. et al. New soft X-ray beamline BL07LSU at SPring-8. *JJournal of Synchrotron Radiation* **2014**, *21*, 352–365.

21. Neppl, S. et al. Capturing interfacial photoelectrochemical dynamics with picosecond time-resolved X-ray photoelectron spectroscopy. *Faraday Discussions* **2014**, *171*, 219–241.

22. Costantini, R.; Stredansky, M.; Cvetko, D.; Kladnik, G.; Verdini, A.; Sigalotti, P.; Cilento, F.; Salvador, F.; De Luisa, A.; Benedetti, D.; Floreano, L.; Morgante, A.; Cossaro, A.; Dell'Angela, M. ANCHOR-SUNDYN: A novel endstation for time resolved spectroscopy at the ALOISA beamline. *Journal of Electron Spectroscopy and Related Phenomena* **2018**, *229*, 7–12.

23. Chan, W.-L.; Ligges, M.; Jailaubekov, A.; Kaake, L.; Miaja-Avila, L.; Zhu, X.-Y. Observing the Multiexciton State in Singlet Fission and Ensuing Ultrafast Multielectron Transfer. *Science* **2011**, *334*, 1541–1545.

24. Wilson, M. W. B.; Rao, A.; Clark, J.; Kumar, R. S. S.; Brida, D.; Cerullo, G.; Friend, R. H. Ultrafast dynamics of exciton fission in polycrystalline pentacene. *Journal of the American Chemical Society* **2011**, *133*, 11830–11833.

25. Pensack, R. D.; Ostroumov, E. E.; Tilley, A. J.; Mazza, S.; Grieco, C.; Thorley, K. J.; Asbury, J. B.; Seferos, D. S.; Anthony, J. E.; Scholes, G. D. Observation of Two Triplet-Pair Intermediates in Singlet Exciton Fission. *Journal of Physical Chemistry Letters* **2016**, *7*, 2370–2375.

26. Marciniak, H.; Fiebig, M.; Huth, M.; Schiefer, S.; Nickel, B.; Selmaier, F.; Lochbrunner, S. Ultrafast Exciton Relaxation in Microcrystalline Pentacene Films. *Physical Review Letters* **2007**, *99*, 176402.

27. Costantini, R.; Faber, R.; Cossaro, A.; Floreano, L.; Verdini, A.; Hättig, C.; Morgante, A.; Coriani, S.; Dell'Angela, M. Picosecond timescale tracking of pentacene triplet excitons with chemical sensitivity. *Communications Physics* **2019**, *2*, 56.

28. Zheng, Z.; Tummala, N. R.; Fu, Y. T.; Coropceanu, V.; Brédas, J. L. Charge-Transfer States in Organic Solar Cells: Understanding the Impact of Polarization, Delocalization, and Disorder. *ACS Applied Materials and Interfaces* **2017**, *9*, 18095−18102.

29. Tritsch, J. R.; Chan, W.-L.; Wu, X.; Monahan, N. R.; Zhu, X.-Y. Harvesting singlet fission for solar energy conversion via triplet energy transfer. *Nature Communications* **2013**, *4*, 1−7.

# 2 Experimental details

In this chapter I will briefly describe the techniques employed in the measurements reported in this thesis and give a detailed overview on the experimental setup, whose development represented the first significant achievement of my PhD project.
I will begin by presenting the photoelectron spectroscopies I used, namely X-ray and ultraviolet photoemission (XPS and UPS) and two-photon photoemission (2PPE). All these techniques are photon-in/electron-out spectroscopies which allow to measure different properties of the sample, depending on the photon source that is used. A second section will be dedicated to X-ray absorption (XAS) which, as opposed to XPS and UPS, is used to probe the empty states of the sample. Finally I will describe the ANCHOR-SUNDYN endstation, in which these techniques can be performed in a pump-probe fashion by exploiting the pulsed nature of synchrotron radiation.

## 2.1 Photoelectron spectroscopies

When talking about photoelectron spectroscopies it is worth mentioning a few names that contributed to the history of physics. The photoelectric effect was first observed by Heinrich Hertz in 1887[1] and in 1905 it was explained by Albert Einstein[2]. Two years later, in 1907, the first XPS spectra were presented by P.D. Innes[3] (J.J. Thomson's PhD student), and after half a century of technical improvements Kai Siegbahn recorded the first high resolution spectrum[4]. Nowadays, XPS is routinely performed in a huge number of laboratories and it is one of the most widely used techniques in surface science.
When a sample is exposed to electromagnetic radiation with a sufficiently short

wavelength, photoelectrons are emitted from the material. Moreover, if a high-power laser is used as a source, photoemission can be achieved even if the photon energy is below threshold. With the huge photon densities that are typical of pulsed lasers nonlinear processes can occur, and this is the case of two-photon photoemission (2PPE).

### 2.1.1 X-ray and ultraviolet photoemission

A standard photoemission measurement consists in exposing the sample to a monochromatic radiation, with energy hν, and then observing the distribution of the emitted electrons as a function of their kinetic energy, $E_k$, which will be given by:

$$E_k = h\nu - E_B - \Phi \tag{2.1}$$

where $E_B$ is the binding energy of the state from which the photoelectron was emitted and $\Phi$ is the work function of the sample. Depending on the photon energy used for the measurement we will be talking about UPS, which is performed with ultra-violet sources (10 - 100 eV), or XPS, which is performed with X-ray sources (> 100 eV). UPS and XPS can be successfully performed in laboratories exploiting conventional sources such as helium discharge lamps ($h\nu$ = 21.2 eV) and X-ray tubes (e.g. Al $K_\alpha$, $h\nu$ = 1487 eV). On the other hand, both techniques take great advantage of the higher photon flux and energy tunability of synchrotron light sources. Clearly, the photon energy used defines the limit of the binding energy that can be probed: with UPS only the valence band is mapped, while for characterizing the core levels of a sample a XPS analysis is required. The process is illustrated in Figure 2.1.

XPS spectra are commonly used for determining the sample composition, as each atom displays a unique set of core levels with distinctive binding energies. Moreover, the same core level can be found at slightly different binding energies depending on the chemical state and the environment surrounding the emitting atom. By analyzing the chemical shifts, it is therefore possible to distinguish between inequivalent atoms of the same element as well as to gather information about the interactions an atom may be involved in. UPS spectra, instead, carry information about the valence band states of the system. Even if the technique is less chemically sensitive due to the intrinsic nature of the valence states, it is a

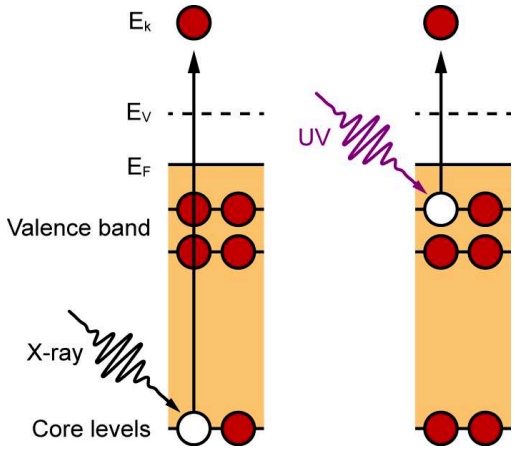


**Figure 2.1 | Energy diagram of the photoemission process.** In XPS (left) a monochromatic X-ray beam is used to ionize the core electrons, which are then detected as a function of their kinetic energy ($E_k$). UPS (right) is typically used to measure the valence band of the sample, as photons with energy in the UV range are not sufficient to eject the core electrons.

fundamental tool for characterizing the optical and electronic properties of the sample. In particular, the angular distribution of the UPS signal allows mapping the dispersion of the valence band states.

A crucial property of photoemission is surface sensitivity. The escape depth of photoelectrons is related to their inelastic mean free path, which is in the order of 10 Å for electrons with $E_k$ = 20 - 1000 eV, meaning that the electrons detected in this kinetic energy range were emitted from the first few layers of the sample. This is the reason why XPS and UPS are among the most popular tools for characterizing thin films and molecular adsorbates. A more detailed description of these techniques can be found elsewhere[5].

## 2.1.2 Two-photon photoemission

The development of lasers in the 1960s brought a renewed interest in the topic of photoemission. It was soon observed that laser beams could trigger electron emission from solids even with photon energies below the work function. These first experiments were interpreted as thermionic emission due to laser induced heating[6,7], but theoretical calculations demonstrated that nonlinear optical effects were also possible[8]. The clear evidence of multiphoton photoemission from

sodium was reported in 1964[9], when the use of pulsed GaAs lasers allowed to remove thermal effects from the equation. In the following years, the considerable improvements in laser technology led to the development of a new approach in spectroscopy: pump-probe. In such experiments a first laser pulse is used to pump the sample to an excited state, and the evolution of the system is then probed by a delayed pulse. The first example of time-resolved two-photon photoemission (TR-2PPE) measurement was carried out on ZnTe crystals in 1982 with 5 ps resolution[10], and the availability of progressively shorter laser pulses soon brought the resolution to the 10 fs scale, allowing the characterization of the short-lived image-potential states in metals[11].

Unlike traditional photoemission, which is a one-photon mechanism, 2PPE is a

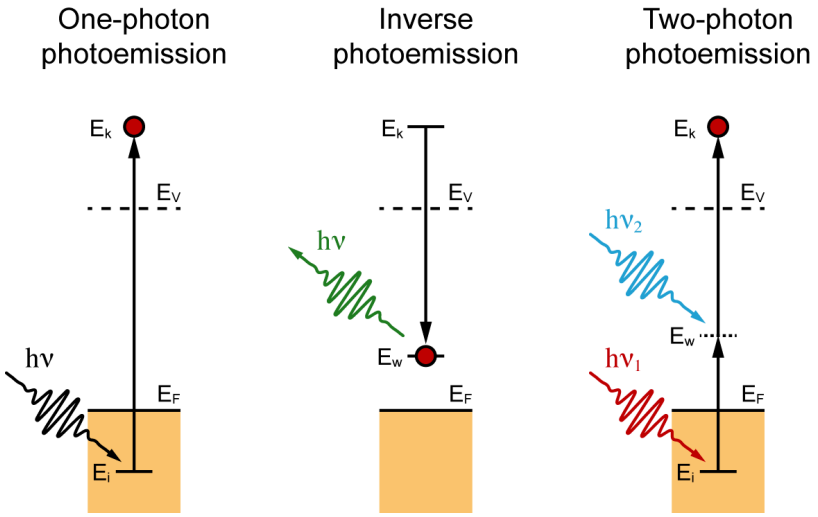


**Figure 2.2 | Two-photon photoemission compared to standard and inverse photoemission.** In traditional photoemission (left) the kinetic energy distribution of the emitted electrons is used to characterize the occupied states of the sample. In inverse photoemission (center) the process is reversed and the density of unoccupied states is probed by directing a low energy electron beam on the sample and detecting the spectrum of emitted photons. In 2PPE (right) a first photon ($h\nu_1$) promotes an electron from an occupied state to an intermediate unoccupied state ($E_w$) and a second photon ($h\nu_2$) is used to ionize the previously excited electron with a kinetic energy $E_k$. Wavelength dependent measurements can be performed to assign the different resonances in 2PPE spectra to either occupied or unoccupied states of the sample.

second-order process capable of characterizing both occupied and initially unoccupied states. It is therefore a valid alternative to the traditionally used inverse

photoemission (IPS), which requires a more complicated apparatus and typically offers a limited energy resolution (few 100 meV). As illustrated in Figure 2.2, in 2PPE a first pulse (i.e. the pump, $h\nu_1$) excites the electrons from below the Fermi level ($E_F$) of a metal substrate (or from an initially occupied adsorbate state) into an intermediate state ($E_w$). The excited-state electrons are then ionized with a second pulse (i.e. the probe, $h\nu_2$) and detected as a function of their kinetic energies as in conventional photoemission spectroscopies. Of course, both $h\nu_1$ and $h\nu_2$ are required to be smaller than the work function of the sample to avoid direct photoemission, which would cause background subtraction issues for the 2PPE signal. If the initial excitation promotes an electron into a real intermediate state, its lifetime can be determined by delaying the probe pulse with respect to the pump and monitoring the decrease of the photoemission signal with increasing delay time. On the other hand, excitations via a virtual intermediate state result in much faster decays that are typically used to measure the cross-correlation of the two pulses, which defines the temporal resolution for the measurements of real excited states. A common benchmark for this purpose is 2PPE from the Cu(111) surface state[12].

Furthermore, to determine the occupancy of the states that appear in a 2PPE spectrum, a wavelength dependency measurement can be performed. If pump and probe energies are changed by $h\delta\nu_1$ and $h\delta\nu_2$, respectively, the kinetic energies of the photoelectrons emitted from an initially occupied state will vary by $h(\delta\nu_1+\delta\nu_2)$. On the other hand, the lines corresponding to initially unoccupied states will be shifted only by $h\delta\nu_2$, because the position of the intermediate state is well-defined with respect to the vacuum level, if a continuum of initially occupied states is available. Wavelength tunability can be achieved through different approaches. Ti:Sapphire lasers offer a tunable output in the red (> 700 nm) and near-IR range, which can be extended in the visible and UV regions via high harmonic generation or by using an optical parametric amplifier (OPA). Another popular solution is represented by doped yttrium aluminum garnet (YAG) lasers, which yield an almost monochromatic IR beam (around 1030 nm) with a pulse energy usually one to two orders of magnitude higher than Ti:Sapphires operating at similar repetition rates (0.1-1 MHz), albeit with a typically higher pulse width (> 100 fs). With doped YAG lasers an OPA can be used to tune the output wavelength from UV ($\sim$ 200 nm) to near-IR ($\sim$ 2500 nm). In both cases, for

time-resolved 2PPE dichroic mirrors are used to separate pump and probe beams and the variable delay between the two pulses is introduced through a motorized translation stage. Additional details and possible applications of 2PPE are reported in recent reviews[13,14].

## 2.2 X-ray absorption

In this section I will briefly describe near edge X-ray absorption fine structure, commonly known as NEXAFS, or alternatively just XAS. For a complete review about principles, techniques and applications of NEXAFS spectroscopy see Stöhr's book[15].

NEXAFS was developed in the 1980s as a tool for investigating the structural properties of low-Z molecules adsorbed on surfaces, systems in which the use of X-ray diffraction was rather limited due to the low abundance of species and in some cases to the lack of periodicity. NEXAFS spectra are obtained by scanning the photon energy around the absorption edge of a certain element, thus a tunable X-ray source like a synchrotron is an essential requirement for this technique. To a first approximation, the measured absorption spectrum will be proportional to the X-ray absorption cross section: $\sigma_{\mathrm{x}}$. Such quantity is defined as the number of electrons excited per unit time divided by the number of incident photons per unit time per unit area, and can be calculated from Fermi's Golden Rule. In particular, for a transition from an initial state $|i\rangle$ to a final state $|f\rangle$ driven by a plane electromagnetic wave with vector potential $\mathbf{A} = \boldsymbol{\eta} A_0 \, e^{i(\mathbf{k}\cdot\mathbf{x} - wt)}$, under the dipole approximation one can obtain:

$$\sigma_{\mathrm{x}} \propto |\, \langle f |\, \boldsymbol{\eta} \cdot \mathbf{p} \,| i \rangle \,|^2 \, \rho_f(E) \tag{2.2}$$

where $\boldsymbol{\eta}$ is the polarization unit vector, $\mathbf{p}$ is the sum of the linear momentum operators of the electrons and $\rho_f(E)$ is the energy density of final states. In NEXAFS, the initial state $|i\rangle$ is generally a localized atomic core level, while $|f\rangle$ can represent either a bound or a continuum state. A picture of the absorption process from a diatomic molecule is shown in Figure 2.3. If we focus on the pre-edge region, we may notice that the absorption spectrum is dominated by transitions to unoccupied molecular orbitals (UMOs), while transitions to the continuum

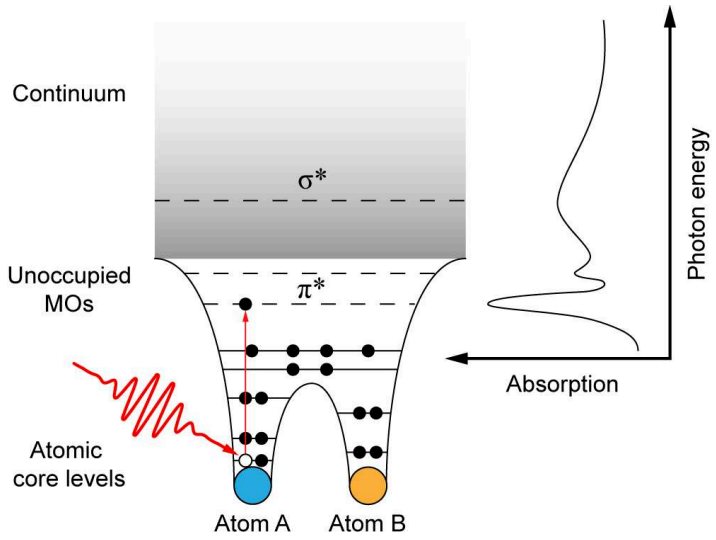


**Figure 2.3 | X-ray absorption spectroscopy on a diatomic molecule.** When scanning the photon energy of the incoming beam through an absorption edge of the atom A we may detect a structured absorption signal, due to transitions from the localized core level to unoccupied molecular orbitals (MOs). By analizing the fine structure of NEXAFS spectra both chemical and structural information on the system can be extracted.

will start contributing to the signal as the photon energy approaches the ionization potential. A detailed analysis of the fine structure of NEXAFS spectra may be used to extract information on the electronic properties of the adsorbate, but for complex molecules non-trivial theoretical calculations may be required. On the other hand, with polarization dependent measurements the absorption geometry can be readily determined.

A model for extracting the molecular orientation on surfaces from angular dependent NEXAFS was presented by Stöhr and Outka in 1987[16]. Molecular orbitals are highly directional and are commonly distinguished in $\pi^*$, oriented orthogonally to the corresponding bond, and $\sigma^*$, oriented along the bond. If we recall Equation 2.2, for the dipole selection rules we have that a transition from a 1s orbital, which has a spherical symmetry, to either a $\pi^*$ or $\sigma^*$ state is more favorable if the polarization vector, $\boldsymbol{\eta}$, of the incoming beam is directed along the final state orbital. Therefore, in NEXAFS the molecular orientation with respect to the surface can be quantitatively determined by mapping the intensity of near-edge resonances as a function of the angle between the sample normal and

the polarization of the incoming beam. With nearly linear or planar molecules a rough estimate of the orientation can be extracted by acquiring two spectra, one in *p* and one in *s* polarization[†], and observing the dichroism of the $\pi^*$ peaks: if the molecule is lying mostly flat on the surface $\pi^*$ resonances will have maximum intensity in the *p* configuration. Analogous considerations apply to $\sigma^*$ peaks.
Several methods can be employed for detecting the NEXAFS signal, but when dealing with low-Z molecules adsorbed on surfaces the most suitable approach is to measure the Auger electron yield (AEY). After the absorption of an X-ray photon the system is left with a core hole, and the Auger decay is the most favorable recombination process for K-edge absorption in low-Z atoms. Moreover, as already mentioned for photoemission, the escape depth of the electrons is limited to a few molecular layers, thus ensuring a high surface sensitivity.

## 2.3 The ANCHOR-SUNDYN experimental setup

The ANCHOR-SUNDYN setup is the result of a collaboration between two projects funded by the Italian Ministry of University and Research (MIUR). The ANCHOR project was financed in 2011 for the spectroscopic and morphologic characterization of hetero-organic assemblies of functionalized molecules, while the more recent SUNDYN project was financed in 2015 with the aim of studying the electronic dynamics in organic-based systems by means of optical pump – X-ray probe experiments. An article on the development of the ANCHOR-SUNDYN setup has recently been published on the Journal of Electron Spectroscopy and Related Phenomena[17], the technical details that are relevant for this thesis are reported in the next few pages.

### 2.3.1 ANCHOR

The ANCHOR endstation has been set up on the HASPES branchline of the ALOISA beamline at the Elettra Synchrotron in Trieste. HASPES uses the first part of the optics of the ALOISA beamline where a plane mirror-plane grating

[†]Conventionally, *p* polarization denotes a configuration in which the electric field is parallel to the plane of incidence, while it is perpendicular in *s* polarization.

(PMPG) monochromator is placed after a paraboloidal mirror (collimator) working at grazing incidence (0.5°, i.e. deviation of 1°) and sagittal focusing. The collimator has the focus directly at the center of the undulator (21 m upstream) thus producing a collimated beam on the dispersive system[18]. The collimated and energy-dispersed beam after the PMPG is alternatively focused towards the exit slits of the ALOISA endstation or those of the HASPES branchline. On the main beamline the focusing (at 3 m) is achieved by a second paraboloidal mirror in sagittal focusing and grazing incidence (0.5°). On the branchline, the combination of both much larger deviation angle (6.5°) and focus distance (14 m) allowed us to employ a toroidal mirror to approximate the slope of a paraboloidal mirror (the latter having an intrinsic slope error much larger than that of toroidal mirrors, in our case 5 arcsec vs 1 arcsec, respectively). Given the low divergence (0.3 mrad) of the beam at the HASPES exit slits (ES), no refocusing mirror is needed and the experimental endstations can be mounted directly after the ES chamber. In particular, the ANCHOR endstation is mounted 1 m behind the ES chamber, which is integrated with a built-in windowless gas ionization chamber for the energy calibration and resolution characterization of the photon beam. The incidence angle on the toroidal focusing mirror (3.25°) limits the highest photon energy to 1200 eV (minimum photon energy 140 eV) with respect to the ALOISA beamline (designed to operate up to 8 keV). On the other hand, the absence of a refocusing mirror yields a slightly larger flux (10 to 20%) at the branchline, while preserving the same energy resolution of the beamline, which guarantees a resolving power (RP) exceeding $\sim 5000$ from 250 to 900 eV in standard working conditions ($0.5 - 1 \times 10^{12}$ photons/s)[19]. Finally, the spot size at the HASPES exit slits is $350 \times 60\ \mu m^2$ (horizontal $\times$ vertical), which translates to $500 \times 200\ \mu m^2$ at the sample position in the ANCHOR chamber (max RP $\sim 2000$).

The ANCHOR endstation has been designed to perform in-situ growth and characterization of organic thin films. A scheme of the experimental setup is shown if Figure 2.4. High resolution XPS and NEXAFS are typically employed for the chemical analysis of the samples. The chamber is also equipped with a monochromatic X-ray source (Omicron XM1000 MkII) and a helium discharge lamp (Omicron HIS 13) which are used for a complementary characterization of the systems and offline measurements. The X-ray source can be operated

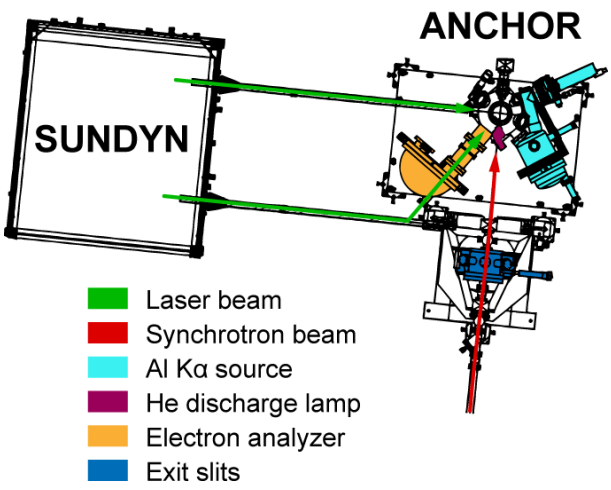


**Figure 2.4 | Technical drawing of the ANCHOR endstation and of the coupling to the SUNDYN laser.** The two additional optical breadboards mounted near the UHV chamber for beam alignment and focusing are not shown for clarity, just the possible beam paths are indicated.

with two filaments of different length, providing a spot size of $1\times3\,\mathrm{mm}^2$ and $1\times5\,\mathrm{mm}^2$, respectively. The emission power is 300 W. Typical XPS spectra on molecular monolayers with the Omicron source require 8 - 10 hours of acquisition to display a reasonable signal-to-noise ratio. The helium lamp is used for the UPS analysis. For this source the spot size on the sample is $4\times4\,\mathrm{mm}^2$, and the photon flux is in the range of $10^{10}$ photons/s. Photoelectrons at ANCHOR were originally detected via a 120 mm hemispheric electron analyzer (PSP Vacuum, Resolve 120), which has been recently upgraded to a 150 mm analyzer (SPECS, Phoibos 150). A 2D delay-line detector, developed for time-resolved experiments by the Elettra Electronic Lab[20], was installed on both analyzers. A variable temperature (200 - 900 K) sample holder is mounted on a 5-axis manipulator (VG), and a load-lock system is also present for fast sample replacement. The polar angle of the manipulator can be rotated through a stepper motor (0.1° resolution), to perform angle-resolved UPS measurements. Both the chamber setup and the sample holder have been developed in-house. The system operates in ultra-high vacuum (UHV) conditions, with a typical base pressure of $3\times10^{-10}$ mbar. Sample growth is performed in-situ via physical vapor deposition (PVD) either through effusion cells or Pyrex vials. A LabVIEW software package has been developed for data acquisition and for controlling the beamline optics.

### 2.3.2 SUNDYN

The latest addition to the setup is the SUNDYN laser, which is a Yb:YAG fiber laser (Amplitude Systèmes, Tangerine HP), with a fundamental wavelength of $1030 \pm 5$ nm. Non-linear beta barium borate (BBO) crystals are used for generating higher harmonics up to the 4th (that is: 515, 343 and 257 nm). The laser can be operated at repetition rates between 175 kHz and 2 MHz, by selecting integer sub-multiples of the feeding oscillator frequency of 41.6 MHz. In this range, the average output power is slightly higher than 35 W, consequently, the pulse energy ranges from 200 µJ to $\sim$ 18 µJ, while the pulse width can be varied from 310 fs to 10 ps by detuning the pulse compressor. An essential feature of our laser system is the module for the synchronization of the oscillator to an external source (i.e. the Elettra storage ring) and its integrated phase shifter that allow us to vary the delay between synchrotron and laser pulses. Moreover, in order to have full wavelength tunability in the 210 - 2600 nm range we installed an optical parametric amplifier (Amplitude Systèmes, Mango OPA), which has been configured for operating at 385 kHz. As can be seen in Figure 2.4, SUNDYN optical table lies near the ANCHOR endstation and the optical beam can be delivered into the UHV chamber through two different UVFS windows at an angle of 90° or 35° with respect to the incoming synchrotron beam. The 35° configuration has been scarcely used, as it requires to focus the beam through the hemispherical analyzer entrance slits, limiting the spot size at the sample to $\sim 700 \times 300$ µm$^2$ which, if compared to the $200 \times 200$ µm$^2$ focus that can be set in the 90° configuration, means a factor of $\sim 5$ in the maximum achievable fluence. A scheme of the actual optical setup is shown in Figure 2.5. The 41.6 MHz oscillator pulses are delivered to the amplifier via an optical fiber and, after the reduction of the repetition rate operated by the pulse picker, the signal is amplified and the output is split into two beams by means of a waveplate and a polarizing beam splitter. The waveplate is set in order to deflect 26 W as an input for the OPA, while the remaining $\sim 10$ W are transmitted into the harmonics module, which delivers the 257 nm beam (4th harmonic, $\sim 0.9$ W) that is typically used as a probe for 2PPE measurements. A motorized linear translation stage (300 mm range, 0.31 µm resolution) is placed in the optical path of the 4th harmonic beam to vary the delay between the pump and probe pulses. The two

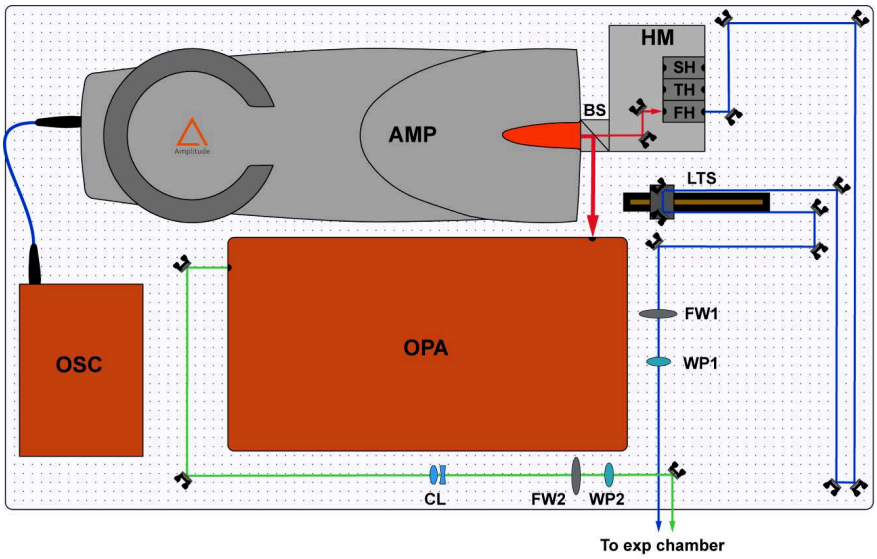


**Figure 2.5 | Laser setup.** The 41.6 MHz oscillator (OSC) pulses are sent to the amplifier (AMP) via optical fiber. The repetition rate is reduced to the desired value by an internal pulse picker, and a polarizing beam splitter (BS) deflects 26 W of the 1030 nm output to pump the optical parametric amplifier (OPA). The OPA is used to generate the pump beam in the 210 - 2600 nm range. The remaining power ($\sim$ 10 W) of the amplifier output is transmitted by the beam splitter to the harmonics module (HM), in which the fourth harmonic (FH) is generated. The FH is sent through a linear translation stage (LTS) which is used to vary the delay between pump and probe pulses in 2PPE measurements. The two beams are recombined in a quasi-collinear geometry before being sent to the experimental chamber. Neutral density filter wheels (FW) and half-waveplates (WP) are inserted in the optical path of both beams to adjust their intensity and polarization. On the pump beam path a pair of collimating lenses (CL) is also inserted to compensate for the divergence of the OPA output.

beams are then directed in a quasi-collinear geometry ($\sim 5°$) to a second breadboard mounted near the experimental chamber, where two different pairs of mirrors and lenses are used to ensure a proper overlap of the beams on the sample. Additional elements on the optical table include half-waveplates and neutral density filter wheels for both pump and probe beams, to adjust their polarization and intensity, and a pair of collimating lenses to compensate for the divergence of the OPA output, which is in the order of few mrads.

### 2.3.3 Time-resolved X-ray spectroscopies

In laser-based time-resolved measurements the synchronization of pump and probe pulses is automatically achieved by splitting the output beam of a single laser source, and the delay time between the two is easily varied through motorized translation stages. A more complicated scheme is required for optical pump – X-ray probe experiments, as the pump laser has to be synchronized with a different probe source. Over the past two decades, the pump-probe approach has been applied with different types of pulsed X-ray sources, such as free-electron lasers (FELs)[21–27], high harmonic generation facilities (HHGs)[28–30] and synchrotrons[31–34]. The vast majority of the current operational setups for pump-probe X-ray spectroscopies, however, relies on photon detectors, thus limiting the possible means of probing the chemical and electronic dynamics of the samples to the bulk sensitive NEXAFS measured in fluorescence yield. The use of time-resolved XPS instead, is much more limited and, due to repetition rate and pulse energy requirements, is more suitable to synchrotron facilities. To date, time-resolved XPS can be performed in just a few synchrotron beamlines, i.e. PM4[35] at BESSY II, TEMPO[36] at SOLEIL, BL07LSU[37] at SPring-8 and 11.0.2[38] at ALS, as an evidence of the fact that the development in this area of research is still at an early stage. With the ANCHOR-SUNDYN endstation we aim at contributing to the technical advancement in time-resolved X-ray spectroscopies by providing a new experimental setup in which both NEXAFS and XPS can be performed in a pump-probe fashion with sub-ns temporal resolution and a fully tunable pump wavelength in the 210 - 2600 nm range.

The scheme of the time-resolved setup at the ANCHOR-SUNDYN endstation is illustrated in Figure 2.6. Here, the synchronization is ensured by using the 499.65 MHz radio frequency (RF) signal of the Elettra storage ring as a clock for the laser oscillator. The same RF signal is also processed through a jitter cleaner (Silicon Labs, Si5317) and a frequency divider (Analog Devices, AD9516) to generate the trigger signal for the delay-line detector. Due to the finite flight time of low energy electrons in the hemispheric analyzer, it is not possible to completely discriminate the electrons emitted from the consecutive pulses normally delivered in the multibunch (MB) operation, which are separated by 2 ns. To overcome this limitation, special filling modes of the storage ring are required

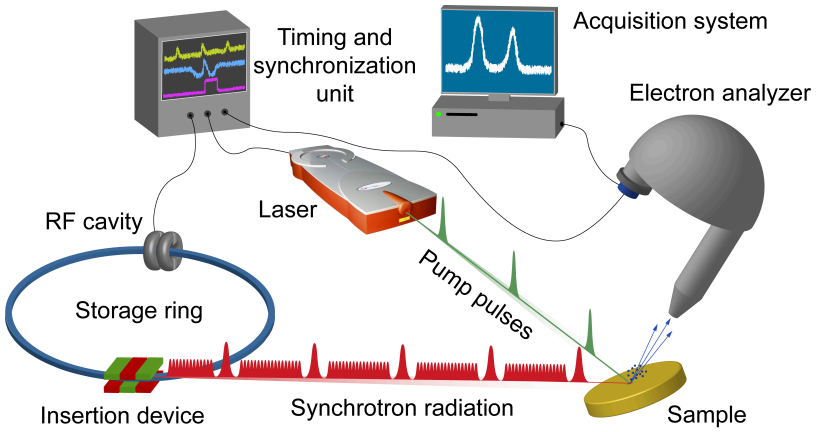


**Figure 2.6 | Ilustration of the ANCHOR-SUNDYN time-resolved setup.** The radio frequency (RF) signal of the storage ring is used to synchronize both the laser and the acquisition system to the synchrotron radiation pulses. A timing unit has been developed for monitoring the synchronization of the pulses during time-resolved measurements.

for time-resolved measurements. As other similar synchrotrons[38–40], Elettra can operate in single bunch (SB) or in a hybrid bunch (HB) mode. In detail, in HB a single electron bunch is placed in the 150 ns dark gap that is present in the multibunch distribution[31], providing 120 ps FWHM X-ray pulses with 1.157 MHz repetition rate, which is the revolution frequency of the storage ring. On the other hand, in SB only one bunch per revolution is injected. A shorter pulse is available in SB ($\sim$ 60 ps FWHM), because the superconductive 3rd harmonic cavity (3HC), which is used in normal and hybrid mode operation for stretching the electron bunches to ensure a more stable beam[41], is not necessary for this low current mode. Clearly, the low ring current in SB, i.e. 5 mA vs the 300 mA of HB, represents an issue for most of the users at a synchrotron facility, who typically apply for a beamtime for the high photon flux. The HB is therefore the preferred operation mode, while the SB is available only on a few limited occasions. In both cases, the count rate when detecting only the single bunch will be roughly 100 times lower if compared to standard multibunch measurements.

The filling pattern at Elettra and the ANCHOR-SUNDYN pump-probe scheme are reported in Figure 2.7a. For time-resolved experiments the laser is run at 385.67 kHz, meaning that one hybrid pulse every 3 revolutions is pumped. This fact allow us to acquire both pumped (P) and unpumped (U) signal in the same

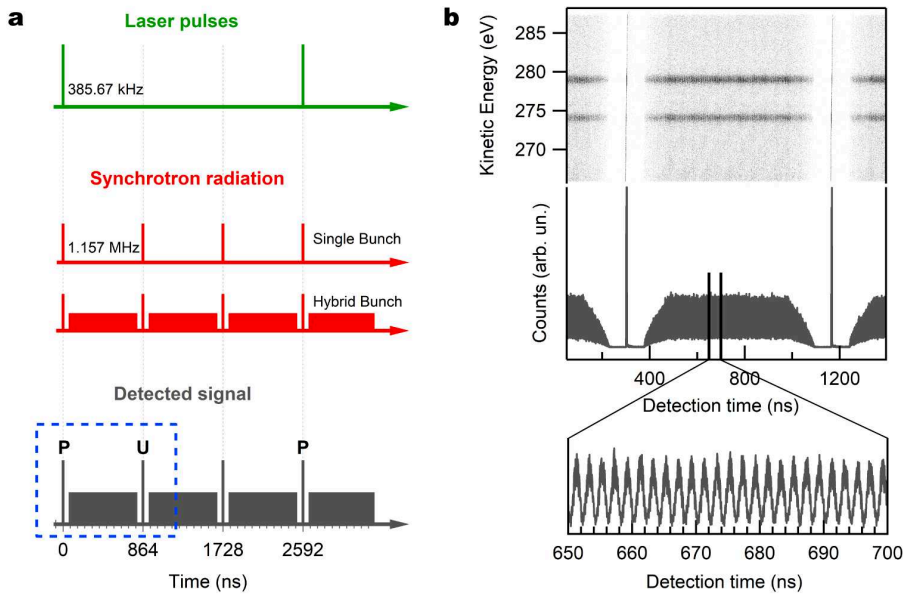


**Figure 2.7 | Scheme for pump-probe experiments at Elettra. a** the 385.67 kHz laser pulses are used to pump one single or hybrid bunch every three revolutions. By opening a 1.5 $\mu$s acquisition window (blue dashed box) a pumped (P) and an unpumped (U) synchrotron pulses can be detected simultaneously. **b** real acquisition window for Ag3d lines measured with hv = 650 eV and a pass energy of 250 eV. The top graph shows a false color plot of photoemission counts as a function of kinetic energy and arrival time on the detector, while the energy integrated distribution is plotted below. The hybrid filling pattern of the storage ring is clearly distinguishable, and the high pass energy also allows to identify the 500 MHz modulation of the multibunch signal (expanded graph).

$\sim$ 1.5 µs window (blue dashed box in Figure 2.7a), offering a quick normalization procedure by plotting the data as P-U or (P-U)/U, provided that no laser-induced microsecond dynamics are present. Figure 2.7b shows an actual acquisition window for the Ag3d photoemission lines measured on a clean Ag(111) crystal with a photon energy of 650 eV. The kinetic energy of the analyzer was set to 278 eV with a pass energy of 250 eV. Both the position and the arrival time of the electrons on the delay-line detector are recorded, allowing us to fully characterize the temporal structure of the signal. The hybrid bunch filling pattern is clearly visible, and at this high pass energy even the 2 ns spacing in the multibunch is preserved. Still, the signal is not completely zeroed between consecutive pulses, making it impossible to exploit the electrons photoemitted by the multibunch for time-resolved experiments, therefore, during the acquisition of a spectrum, the

multibunch signal is discarded and only the hybrid bunches are considered in the analysis. It has to be mentioned that, even though the multibunch signal is not recorded, the photon flux on the sample is unavoidably high and strongly contributes to the sample radiation damage, especially in case of organic films. In a similar setup at the BESSY II synchrotron, a MHz chopper was developed to transmit only the hybrid pulses and to completely dump the multibunch photons, thus minimizing the radiation dose[35,42].

Once the synchronization between laser and synchrotron is achieved, the spatial and temporal overlap on the sample need to be determined as a first step in any experiment. A frequent approach consists in detecting vacuum space charge effects in the photoemission spectra. As already mentioned in Section 2.1.2, when an intense optical pulse impinges on the sample a cloud of low energy electrons is emitted due to multiphoton effects. Such electron cloud is responsible for the broadening and the shift of photoemission lines on timescales of up to few nanoseconds, depending on the pump fluence. These effects are well established in photoemission measurements with pulsed sources like lasers, HHGs and FELs[43]. In our setup, the spatial overlap of the beams is first determined on the surface of a cerium doped YAG ($Y_3Al_5O_{12}$) wafer mounted on the sample holder[‡]. For adjusting and monitoring the temporal overlap we developed a LabVIEW software that is interfaced with the laser oscillator and with a 1 GHz digital oscilloscope (Tektronix, DPO5104b). The user interface of the program is shown in Figure 2.8. The timing of the hybrid pulse is monitored through the bunch filling (BF) signal, which is distributed in the experimental hall together with the RF and reproduces the filling pattern of the storage ring, while for the laser a signal from a built-in photodiode is used. The relative distance between the pulses and the trigger signal for the detector are constantly monitored during a measurement and the software automatically acts as a feedback in case of loss of synchronization. A preliminary temporal overlap is obtained on a reverse biased photodiode (Opto Diode, SXUV5) mounted in the experimental chamber, with a precision that is limited to $\sim 2$ ns by the diode rise time, while finer adjustments can be made by observing space charge shifts. An example is reported in Figure 2.9, which shows the Au4f$_{7/2}$ line of a clean Au(111) surface pumped with 5 mJ/cm$^2$ at 515 nm (2.4 eV) and probed with 140 eV. The pump-probe delay at each step

[‡]Ce:YAG crystals are commonly used as phosphors at synchrotrons and FELs.

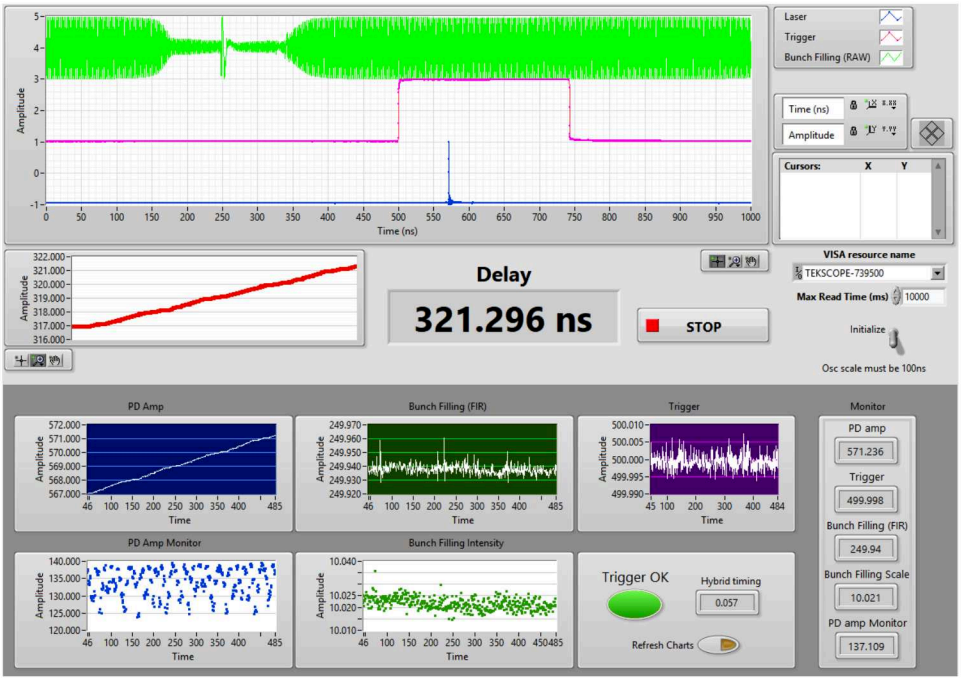


**Figure 2.8 | Screenshot of the LabVIEW software for monitoring the timing of the pulses during normal operation.** The bunch filling (green), laser photodiode (blue) and trigger signal (pink) are displayed in the top graph. Their relative distance is kept constant through a feedback loop, and the actual pump-probe delay is reported in the center of the window. In the bottom panel the timing and amplitude of each signal are monitored separately.

is varied by the integrated phase shifter. Here, negative delay times correspond to the X-ray pulse arriving on the sample before the pump. The space charge shift is maximum (at a fixed pump fluence) when the best spatial and temporal overlap conditions are obtained. The fitted peak positions are plotted as a function of the pump-probe delay in Figure 2.9b, in which the identification of the time zero ($t_0$) is straightforward. The space charge dynamics have been fitted with an exponential decay convoluted with a Gaussian response function (red solid line). A time constant of $0.34 \pm 0.07$ ns is found for the exponential decay at $t > t_0$, which is compatible to the typical timescale of vacuum space charge effects[43]. The dynamics at $t < t_0$ are intrinsically faster (< 1 ps) and the curve is well fitted if the Gaussian broadening (FWHM) is set to 120 ps, the nominal X-ray pulse width in the Elettra hybrid mode. This measurement indicates that the response time, and therefore the temporal resolution of our setup is limited to 120 ps by the X-ray pulse duration, which can be potentially reduced to $\sim 60$ ps when operating

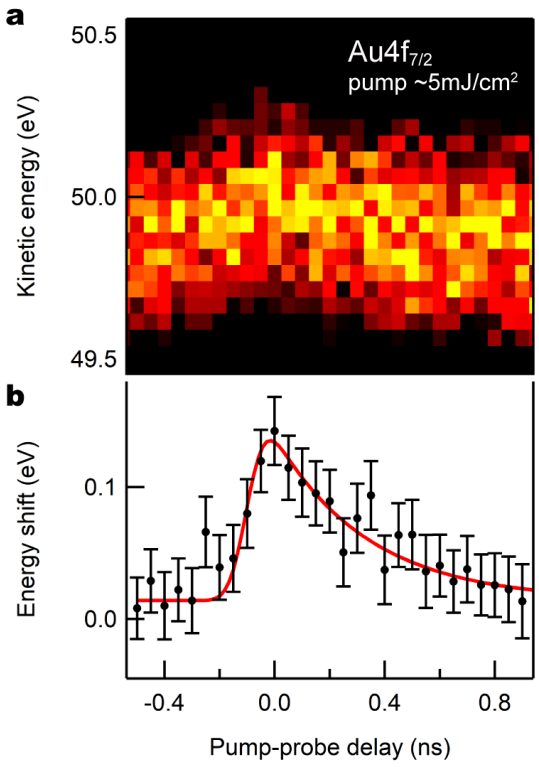


**Figure 2.9 | Space charge shift on the Au4f$_{7/2}$ line. a** False color plot of the photoemission intensity as a function of the kinetic energy and of the pump-probe delay, measured with a 2.4 eV pump and 140 eV probe. **b** Fitted peak shift positions. The red solid line is a fit for the space charge dynamics consisting of an exponential decay convoluted with a Gaussian response function. The 120 ps Gaussian broadening (FWHM) is due to the limited temporal resolution of the system, which is related to the X-ray pulse width. Error bars represent one standard deviation.

in single bunch mode. One last important factor in time-resolved experiments is the jitter between laser and X-ray pulses, which influences the temporal resolution of a measurement over repeated scans. A systematical characterization of the jitter in our setup has yet to be performed, but a reasonable upper limit is set to roughly 50 ps by the overall precision of the LabVIEW software, and this value is consistent with the degree of reproducibility that we are able to achieve in consecutive time scans.

The $\sim$ 100 ps resolution is clearly limiting the processes that can be monitored by means of time-resolved XPS to surface photovoltage effects in semiconductors and slow exciton dynamics in organic films. The general trend to overcome such

limitation is therefore to reduce the synchrotron pulse width to few-ps or even sub-ps with low-alpha modes[36,44] or femtoslicing techniques[45]. On the other hand, shorter pulses are already available at FELs and HHGs but, as only one electron per pulse can be detected, the repetition rate in these facilities represent a limit for photoemission measurements, albeit remaining the best choices for photon-in/photon-out time-resolved experiments. On the FEL's side, a lot of efforts are being put in the development of new facilities with an expected repetition rate in the 0.1 - 1 MHz range[46–48], which will surely compete with synchrotrons in the near future. HHG technology is also experiencing a considerable growth as few setups delivering 40 nm (or $\sim$ 30 eV) pulses at more than 1 MHz have already been reported[49,50], while for higher photon energies (> 300 eV) the repetition rate is still in the few kHz range[51–53]. Nevertheless, it seems only a matter of time until HHG based femtosecond XPS setups will become available and offer a valid alternative to large scale facilities.

In conclusion, I have reported here the technical details and the commissioning of the new ANCHOR-SUNDYN endstation at the ALOISA beamline at Elettra. The setup combines a UHV chamber for *in situ* growth and characterization of organic films with a pulsed laser, allowing to perform sub-ns time-resolved XPS and NEXAFS. A preliminary chemical characterization of the sample can be carried out on the ANCHOR-SUNDYN setup with the UV lamp and the X-ray source that are mounted on the chamber, in order to optimize the sample growth procedure prior to the scheduled beamtimes. Moreover, the current laser setup offers a tunable pump in the 210 - 2600 nm range that can be combined with any of the first four harmonics of the laser (1030, 515, 343 and 257 nm) for measuring the exciton dynamics by means of time-resolved 2PPE with 300 fs resolution. Such measurements are useful for characterizing the excited states lifetime and for defining the pump fluence to be used in time-resolved X-ray spectroscopies. Finally, if we include resonant photoemission spectroscopy (ResPES), in which the valence band is measured at a photon energy resonant with core level excitations, to the list of techniques that are performed in our endstation, we can also have some insights on the ultrafast charge transfer processes that occur on timescales shorter than the core-hole lifetime (tens of fs)[54–58]. ANCHOR-SUNDYN is therefore a compact setup in which the exciton dynamics in organic films can be tracked from the ultrafast (< 50 fs) region in ResPES to

the 0.1 - 100 ns range in pump-probe X-ray spectroscopies, with the 0.3 - 250 ps gap between the two that is covered by time-resolved 2PPE.

# References


1. Hertz, H. Über einen Einfluss des ultravioletten Lichtes auf die electrische Entladung. *Annalen der Physik und Chemie* **1887**, *267*, 983–1000.

2. Einstein, A. Über einen die Erzeugung und Verwandlung des Lichtes betreffenden heuristischen Gesichtspunkt. *Annalen der Physik* **1905**, *322*, 132–148.

3. Innes, P. D. On the Velocity of the Cathode Particles Emitted by Various Metals under the Influence of Rontgen Rays, and Its Bearing on the Theory of Atomic Disintegration. *Proceedings of the Royal Society A: Mathematical, Physical and Engineering Sciences* **1907**, *79*, 442–462.

4. Siegbahn, K.; Edvarson, K. $\beta$-Ray spectroscopy in the precision range of 1 : 105. *Nuclear Physics* **1956**, *1*, 137–159.

5. Fadley, C. S.; Manson, S.; Dill, D. In *Electron spectroscopy: Theory, techniques and applications*; Brundle, C., Baker, A., Eds.; Academic Press London, 1978.

6. Honig, R. E.; Woolston, J. R. Laser-induced Emission of Electrons, Ions, and Neutral Atoms from Solid Surfaces. *Applied Physics Letters* **1963**, *2*, 138–139.

7. Lichtman, D.; Ready, J. F. Laser Beam Induced Electron Emission. *Physical Review Letters* **1963**, *10*, 342–345.

8. Smith, R. L. Two-photon photoelectric effect. *Physical Review* **1962**, *128*, 2225–2229.

9. Teich, M. C.; Schroeer, J. M.; Wolga, G. J. Double-Quantum Photoelectric Emission from Sodium Metal. *Physical Review Letters* **1964**, *13*, 611–614.

10. Williams, R. T.; Royt, T. R.; Rife, J. C.; Long, J. P.; Kabler, M. N. Picosecond time-resolved photoelectron spectroscopy of ZnTe. *Journal of Vacuum Science and Technology* **1982**, *21*, 509–513.

11. Schoenlein, R. W.; Fujimoto, J. G.; Eesley, G. L.; Capehart, T. W. Femtosecond Studies of Image-Potential Dynamics in Metals. *Physical Review Letters* **1988**, *61*, 2596–2599.

12. Ogawa, S.; Nagano, H.; Petek, H. Hot-electron dynamics at Cu(100), Cu(110), and Cu(111) surfaces: Comparison of experiment with Fermi-liquid theory. *Physical Review B* **1997**, *55*, 10869–10877.

13. Weinelt, M. Time-resolved two-photon photoemission from metal surfaces. *Journal of Physics Condensed Matter* **2002**, *14*, R1099–R1141.

14. Szymanski, P.; Garrett-Roe, S.; Harris, C. Time- and angle-resolved two-photon photoemission studies of electron localization and solvation at interfaces. *Progress in Surface Science* **2005**, *78*, 1–39.

15. Stöhr, J. *NEXAFS Spectroscopy*; Springer Series in Surface Sciences; Springer Berlin Heidelberg: Berlin, Heidelberg, 1992; Vol. 25; pp xv, 403.

16. Stöhr, J.; Outka, D. A. Determination of molecular orientations on surfaces from the angular dependence of near-edge x-ray-absorption fine-structure spectra. *Physical Review B* **1987**, *36*, 7891–7905.

17. Costantini, R.; Stredansky, M.; Cvetko, D.; Kladnik, G.; Verdini, A.; Sigalotti, P.; Cilento, F.; Salvador, F.; De Luisa, A.; Benedetti, D.; Floreano, L.; Morgante, A.; Cossaro, A.; Dell'Angela, M. ANCHOR-SUNDYN: A novel endstation for time resolved spectroscopy at the ALOISA beamline. *Journal of Electron Spectroscopy and Related Phenomena* **2018**, *229*, 7–12.

18. Busetto, E.; Lausi, A.; Bernstorff, S. The high-energy monochromator for the ALOISA beamline at Elettra. *Review of Scientific Instruments* **1995**, *66*, 2078–2081.

19. Floreano, L.; Naletto, G.; Cvetko, D.; Gotter, R.; Malvezzi, M.; Marassi, L.; Morgante, A.; Santaniello, A.; Verdini, A.; Tommasini, F.; Tondello, G. Performance of the grating-crystal monochromator of the ALOISA beamline at the Elettra Synchrotron. *Review of Scientific Instruments* **1999**, *70*, 3855–3864.

20. Cautero, G.; Sergo, R.; Stebel, L.; Lacovig, P.; Pittana, P.; Predonzani, M.; Carrato, S. A two-dimensional detector for pump-and-probe and time resolved experiments. *Nuclear Instruments and Methods in Physics Research Section A: Accelerators, Spectrometers, Detectors and Associated Equipment* **2008**, *595*, 447–459.

21. Pietzsch, A.; Föhlisch, A.; Beye, M.; Deppe, M.; Hennies, F.; Nagasono, M.; Suljoti, E.; Wurth, W.; Gahl, C.; Döbrich, K.; Melnikov, A. Towards time resolved core level photoelectron spectroscopy with femtosecond x-ray free-electron lasers. *New Journal of Physics* **2008**, *10*, 033004.

22. Lemke, H. T. et al. Femtosecond x-ray absorption spectroscopy at a hard x-ray free electron laser: Application to spin crossover dynamics. *Journal of Physical Chemistry A* **2013**, *117*, 735–740.

23. Hellmann, S.; Sohrt, C.; Beye, M.; Rohwer, T.; Sorgenfrei, F.; Marczynski-Bühlow, M.; Kalläne, M.; Redlin, H.; Hennies, F.; Bauer, M.; Föhlisch, A.; Kipp, L.; Wurth, W.; Rossnagel, K. Time-resolved x-ray photoelectron spectroscopy at FLASH. *New Journal of Physics* **2012**, *14*, 013062.

24. Ogi, Y. et al. Ultraviolet photochemical reaction of [Fe(III)(C2O4)3]3- in aqueous solutions studied by femtosecond time-resolved X-ray absorption spectroscopy using an X-ray free electron laser. *Structural Dynamics* **2015**, *2*.

25. Nilsson, A.; LaRue, J.; Öberg, H.; Ogasawara, H.; Dell'Angela, M.; Beye, M.; Öström, H.; Gladh, J.; Nörskov, J. K.; Wurth, W.; Abild-Pedersen, F.; Pettersson, L. G. Catalysis in real time using X-ray lasers. *Chemical Physics Letters* **2017**, *675*, 145–173.

26. Dell'Angela, M. et al. Real-Time Observation of Surface Bond Breaking with an X-ray Laser. *Science* **2013**, *339*, 1302–1305.

27. Wernet, P. et al. Orbital-specific mapping of the ligand exchange dynamics of $Fe(CO)_5$ in solution. *Nature* **2015**, *520*, 78–81.

28. Bhattacherjee, A.; Pemmaraju, C. D.; Schnorr, K.; Attar, A. R.; Leone, S. R. Ultrafast Intersystem Crossing in Acetylacetone via Femtosecond X-ray Transient Absorption at the Carbon K-Edge. *Journal of the American Chemical Society* **2017**, *139*, 16576–16583.

29. Kaplan, C. J.; Kraus, P. M.; Ross, A. D.; Zürch, M.; Cushing, S. K.; Jager, M. F.; Chang, H.-T.; Gullikson, E. M.; Neumark, D. M.; Leone, S. R. Femtosecond tracking of carrier relaxation in germanium with extreme ultraviolet transient reflectivity. *Physical Review B* **2018**, *97*, 205202.

30. Zhang, K.; Lin, M. F.; Ryland, E. S.; Verkamp, M. A.; Benke, K.; De Groot, F. M.; Girolami, G. S.; Vura-Weis, J. Shrinking the Synchrotron: Tabletop Extreme Ultraviolet Absorption of Transition-Metal Complexes. *Journal of Physical Chemistry Letters* **2016**, *7*, 3383–3387.

31. Stebel, L.; Malvestuto, M.; Capogrosso, V.; Sigalotti, P.; Ressel, B.; Bondino, F.; Magnano, E.; Cautero, G.; Parmigiani, F. Time-resolved soft x-ray absorption setup using multibunch operation modes at synchrotrons. *Review of Scientific Instruments* **2011**, *82*, 123109–44913.

32. March, A. M.; Stickrath, A.; Doumy, G.; Kanter, E. P.; Krässig, B.; Southworth, S. H.; Attenkofer, K.; Kurtz, C. A.; Chen, L. X.; Young, L. Development of high-repetition-rate laser pump/x-ray probe methodologies for synchrotron facilities. *Review of Scientific Instruments* **2011**, *82*, 073110.

33. Shavorskiy, A. et al. Sub-nanosecond time-resolved ambient-pressure X-ray photoelectron spectroscopy setup for pulsed and constant wave X-ray light sources. *Review of Scientific Instruments* **2014**, *85*.

34. Vankó, G.; Glatzel, P.; Pham, V.-T.; Abela, R.; Grolimund, D.; Borca, C. N.; Johnson, S. L.; Milne, C. J.; Bressler, C. Picosecond Time-Resolved X-Ray Emission Spectroscopy: Ultrafast Spin-State Determination in an Iron Complex. *Angewandte Chemie International Edition* **2010**, *49*, 5910–5912.

35. Giangrisostomi, E.; Ovsyannikov, R.; Sorgenfrei, F.; Zhang, T.; Lindblad, A.; Sassa, Y.; Cappel, U. B.; Leitner, T.; Mitzner, R.; Svensson, S.; Mårtensson, N.; Föhlisch, A. Low Dose Photoelectron Spectroscopy at BESSY II: Electronic structure of matter in its native state. *Journal of Electron Spectroscopy and Related Phenomena* **2018**, *224*, 68–78.

36. Silly, M. G. et al. Pump−probe experiments at the TEMPO beamline using the low-$\alpha$ operation mode of Synchrotron SOLEIL. *Journal of Synchrotron Radiation* **2017**, *24*, 886–897.

37. Yamamoto, S. et al. New soft X-ray beamline BL07LSU at SPring-8. *Journal of Synchrotron Radiation* **2014**, *21*, 352–365.

38. Neppl, S. et al. Capturing interfacial photoelectrochemical dynamics with picosecond time-resolved X-ray photoelectron spectroscopy. *Faraday Discussions* **2014**, *171*, 219–241.

39. Yamamoto, S.; Matsuda, I. Time-Resolved Photoelectron Spectroscopies Using Synchrotron Radiation: Past, Present, and Future. *Journal of the Physical Society of Japan* **2013**, *82*, 021003.

40. Bergeard, N.; Silly, M. G.; Krizmancic, D.; Chauvet, C.; Guzzo, M.; Ricaud, J. P.; Izquierdo, M.; Stebel, L.; Pittana, P.; Sergo, R.; Cautero, G.; Dufour, G.; Rochet, F.; Sirotti, F.; IUCr, Time-resolved photoelectron spectroscopy using synchrotron radiation time structure. *Journal of Synchrotron Radiation* **2011**, *18*, 245–250.

41. Pedrozzi, M. et al. First operational results of the 3rd harmonic superconducting cavities in SLS and ELETTRA. Proceedings of the 2003 Particle Accelerator Conference. 2003; pp 878–880 Vol.2.

42. Förster, D. F.; Lindenau, B.; Leyendecker, M.; Janssen, F.; Winkler, C.; Schumann, F. O.; Kirschner, J.; Holldack, K.; Föhlisch, A. Phase-locked MHz pulse selector for x-ray sources. *Optics Letters* **2015**, *40*, 2265.

43. Hellmann, S.; Rossnagel, K.; Marczynski-Bühlow, M.; Kipp, L. Vacuum space-charge effects in solid-state photoemission. *Physical Review B* **2009**, *79*, 035402.

44. Feikes, J.; Holldack, K.; Kuske, P. Sub-picosecond Electron Bunches in the BESSY Storage Ring. 9th European Particle Accelerator Conference (EPAC 2004) Lucerne, Switzerland, July 5-9, 2004. 2004; pp 1954–1956.

45. Ingold, G. et al. Sub-Picosecond Tunable Hard X-Ray Undulator Source for Laser/X-Ray Pump-Probe Experiments. AIP Conference Proceedings. 2007; pp 1198–1201.

46. Galayda, J. N. The Linac Coherent Light Source-II Project. Proceedings, 5th International Particle Accelerator Conference (IPAC 2014): Dresden, Germany, June 15-20, 2014. 2014; pp 935–937.

47. Röhlsberger, R.; Schroer, C. G.; Wanzenberg, R.; Klumpp, S.; Wurth, W. Light Source Upgrades at DESY: PETRA IV and FLASH2020+. *Synchrotron Radiation News* **2019**, *32*, 27–31.

48. Altarelli, M. The European X-ray Free-Electron Laser: toward an ultra-bright, high repetition-rate x-ray source. *High Power Laser Science and Engineering* **2015**, *3*, 1–7.

49. Cingöz, A.; Yost, D. C.; Allison, T. K.; Ruehl, A.; Fermann, M. E.; Hartl, I.; Ye, J. Direct frequency comb spectroscopy in the extreme ultraviolet. *Nature* **2012**, *482*, 68–71.

50. Hädrich, S.; Krebs, M.; Hoffmann, A.; Klenke, A.; Rothhardt, J.; Limpert, J.; Tünnermann, A. Exploring new avenues in high repetition rate table-top coherent extreme ultraviolet sources. *Light Science & Applications* **2015**, *4*, e320–e320.

51. Bhattacherjee, A.; Leone, S. R. Ultrafast X-ray Transient Absorption Spectroscopy of Gas-Phase Photochemical Reactions: A New Universal Probe of Photoinduced Molecular Dynamics. *Accounts of Chemical Research* **2018**, *51*, 3203–3211.

52. Johnson, A. S.; Miseikis, L.; Wood, D. A.; Austin, D. R.; Brahms, C.; Jarosch, S.; Strüber, C. S.; Ye, P.; Marangos, J. P. Measurement of sulfur L 2,3 and carbon K edge XANES in a polythiophene film using a high harmonic supercontinuum. *Structural Dynamics* **2016**, *3*, 062603.

53. Cousin, S. L.; Silva, F.; Teichmann, S.; Hemmer, M.; Buades, B.; Biegert, J. High-flux table-top soft x-ray source driven by sub-2-cycle, CEP stable, 185-$\mu$m 1-kHz pulses for carbon K-edge spectroscopy. *Optics Letters* **2014**, *39*, 5383.

54. Brühwiler, P. A.; Karis, O.; Mårtensson, N. Charge-transfer dynamics studied using resonant core spectroscopies. *Reviews of Modern Physics* **2002**, *74*, 703–740.

55. Föhlisch, A. Ultrafast charge transfer and nuclear dynamics studied with resonant X-ray spectroscopy. *Applied Physics A* **2006**, *85*, 351–359.

56. Föhlisch, A.; Vijayalakshmi, S.; Hennies, F.; Wurth, W.; Medicherla, V.; Drube, W. Verification of the core-hole-clock method using two different time references: Attosecond charge transfer in c(4×2)S/Ru(0001). *Chemical Physics Letters* **2007**, *434*, 214–217.

57. Cvetko, D.; Fratesi, G.; Kladnik, G.; Cossaro, A.; Brivio, G. P.; Venkataraman, L.; Morgante, A. Ultrafast electron injection into photo-excited organic molecules. *Physical Chemistry Chemical Physics* **2016**, *18*, 22140–22145.

58. Vilmercati, P.; Cvetko, D.; Cossaro, A.; Morgante, A. Heterostructured organic interfaces probed by resonant photoemission. *Surface Science* **2009**, *603*, 1542–1556.

# 3 Exciton fission in pentacene

Over the past decade, the pentacene molecule has been widely studied as a prototypical chromophore for singlet fission, and we decided to adopt it as a test case for the commissioning of our new time-resolved setup. In singlet fission, an optically created singlet exciton is split into two triplet excitons on the sub-ps timescale via an internal conversion process, with the lifetime of the resulting triplet excited states that can extend over a few ns, depending on the crystalline structure of the film. We used time-resolved two-photon photoemission for an initial characterization of the singlet fission dynamics, and we identified the signature of the triplet excited state in the carbon K-edge with transient X-ray absorption measurements. These results were published in Communications Physics[1]. Finally, we performed time-resolved X-ray photoemission spectroscopy with $\sim 100\,\mathrm{fs}$ resolution at the FLASH free-electron laser, which revealed a delayed core level shift that we tentatively attribute to a transient interface dipole generated by the triplet exciton transfer.

## 3.1 Fundamentals of singlet fission

Singlet fission is a photophysical process in which, after an optical excitation, a singlet excited state is converted into two triplet excitons. Its first observation can be dated back to 1965, when it was used to explain the delayed fluorescence in anthracene crystals after laser excitation[2]. A decade later, in 1979, Dexter proposed to exploit the fission process for the sensitization of conventional photovoltaic devices[3], but the idea became more popular only in 2006 when Hanna

and Nozik quantified the actual gains of a singlet fission sensitized solar cell[4], showing that the maximum power conversion efficiency could be pushed beyond the Shockley-Queisser limit[5]. Singlet fission has been observed on a large set of molecules over the past 10 years with the goal of finding the best candidate for applicative purposes, but its implementation on real devices is still elusive. The rich literature on the subject has been summarized in multiple reviews[6–12] and we refer to them for a comprehensive description of the phenomenon, while on the present section my aim is to just provide a general overview of singlet fission, which may be useful for understanding the experimental results that will be presented in the current chapter.

In an oversimplified view, singlet fission in a molecular crystal can be seen as a two-step process as reported in Equation 3.1[13–15]. A molecule in an excited singlet state, $S_1$, interacts with a neighboring molecule in the ground state, $S_0$, to form a triplet pair state, $^1(T_1T_1)$, or more concisely $^1(TT)$, which has an overall singlet character. The fission is then completed as the triplet pair is separated into two independent triplets, $T_1$, due to enthalpic and entropic forces[9].

$$S_0 + S_1 \rightleftharpoons {}^1(TT) \rightleftharpoons T_1 + T_1 \tag{3.1}$$

Such kinetic scheme was demonstrated to be incomplete as recent experiments revealed the existence of an additional intermediate step[16,17]. A more correct model should therefore take into account also the evolution of $^1(TT)$ to a different correlated triplet pair, in which the electronic coherence of the two constituent triplets is lost but the spin coherence is maintained. We will use the notation of Scholes and co-workers[17] and write such state as $^1(T\cdots T)$. The singlet fission process can then be written as:

$$S_0 + S_1 \rightleftharpoons {}^1(TT) \rightleftharpoons {}^1(T\cdots T) \rightleftharpoons T_1 + T_1 \tag{3.2}$$

To remain consistent with the assignment of Zhu and co-workers[8] we define the singlet fission rate as the one of forming $^1(T\cdots T)$, which exhibits the same physical and chemical properties of the two individual triplets. A basic requirement for singlet fission to occur is that the energy of the first excited singlet state should be greater than or equal to twice the energy of the triplet, i.e. $E(S_1) \geq 2E(T_1)$. This condition is fulfilled in pentacene and its derivatives, which are well-known

for their high fission yield[16–22] and whose characterization greatly contributed to the understanding of the singlet fission mechanism. To take advantage of singlet fission as a carrier multiplication mechanism, one must be able not only to identify and avoid the recombination pathways that compete with singlet fission, but also to couple the fission chromophore to a proper acceptor material in order to ensure an efficient triplet harvesting.

### 3.1.1 Triplet exciton harvesting

Over the past few years a lot of efforts have been put on the design of new chromophores with improved stability for practical applications[23–28]. As the molecular library of fission chromophores is being updated with new promising materials, the bottleneck for an efficient charge carrier multiplication in prototypal devices is currently represented by the selective harvesting of triplet excitons. Figure 3.1 illustrates a simplified scheme of singlet fission and triplet harvesting kinetics. For effective gains in the power conversion efficiency it is crucial to maximize the triplet transfer to the acceptor while hindering singlet exciton transfer and exciton recombination, which are the main loss channels in singlet

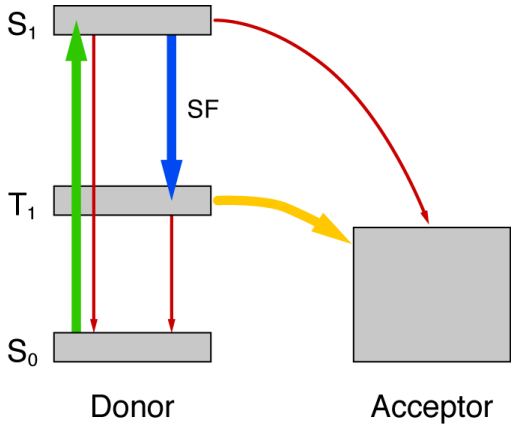


**Figure 3.1 | Simplified view of the singlet fission kinetics and triplet exciton transfer.** After the optical excitation (green), triplet excitons are generated through singlet fission (blue). If the energy levels between the donor and the acceptor are properly aligned, triplet excitons can be harvested (yellow) for producing an enhanced photocurrent. Singlet transfer and exciton recombination are marked with red arrows in the scheme, and they all represent loss channels for the power conversion efficiency of potential devices.

fission based devices. One of the obstacles in triplet harvesting is represented by the small diffusion rate of triplet excitons, which is $\sim 3$ orders of magnitude lower than the one for singlet excitons[29]. As the diffusion length is given by $\sqrt{D\tau}$, where $D$ is the diffusion constant and $\tau$ is the exciton lifetime, the intrinsically longer lifetime of triplet excitons ensures a greater diffusion length, which ideally suggests that the optimal device architecture has to include a high fission yield chromophore with an active layer thickness close to the triplet diffusion length. This design principle led to the first prototypal solar cell based on a 15 nm pentacene film with an external quantum efficiency peaking at 109%[30].

More recently, Huang and co-workers revealed a singlet-mediated triplet diffusion pathway that result in a faster and longer range transport for triplet excitons[31]. Such mechanism is based on the interplay between singlet fission and triplet fusion, which can lead to an effective triplet transport length of $\sim 300$ nm for polycrystalline tetracene[10,32]. Even though singlet fission is slightly endoergic in tetracene, a high fission yield is ensured by the quantum superposition between $S_1$ and $^1(TT)$ states combined with entropic gains[33], and the equilibrium between singlet and triplet exciton populations is maintained by the exoergic triplet fusion. In this model the singlet excitons serve as intermediates that allow fast diffusion and a quick fission back to triplets, so that triplet transfer at the donor/acceptor interface is still the most favorable channel, and can be achieved in the nanosecond timescale. In this perspective, fission-based solar cells should employ an adequately thick layer of a fission chromophore with a small endoergic gap to take advantage of the singlet-mediated diffusion.

Thanks to the huge advances in chemical engineering it has become relatively simple to tune the intermolecular coupling and the molecular packing in organic films, granting reasonable control on singlet fission rates and exciton diffusion[23,34–36], but obtaining efficient charge injection to the electrodes is still challenging. The focus has therefore progressively moved to the interfaces with charge acceptors, and different strategies have been proposed to try to harvest triplet excitons from the fission material: metal oxides[37–39], quantum dots[40–42] and fullerene[30,43–46] are among the most frequent choices. For characterizing the exciton dynamics through the interfaces, laser based pump-probe spectroscopies such as time-resolved two-photon photoemission (TR-2PPE) and transient absorption (TA) are routinely used. Both techniques allow to measure the sub-ps

dynamics in a limited region of the valence and conduction bands close to the Fermi level, and when dealing with a complex device-like architecture the contribution of the different species in TR-2PPE and TA spectra can be difficult to disentangle. Such limitation can be overcome with time-resolved X-ray spectroscopies, as the chemical sensitivity that is obtained by probing the core levels can potentially be exploited to track the exciton diffusion through the interfaces. At the ANCHOR-SUNDYN endstation we put our efforts in developing a setup in which both TR-2PPE and pump-probe X-ray spectroscopies can be performed on the same sample, providing a valid tool for the characterization of triplet excited states dynamics and for the identification of the most promising interfaces for triplet harvesting.

## 3.2 Observing singlet fission: TR-2PPE analysis

As stated in the opening of this chapter we decided to use pentacene as a model system for the commissioning of our new experimental setup, since it has been the most intensely studied singlet fission chromophore. For this purpose, a 2 monolayer (ML) pentacene film was deposited on a $C_{60}$ covered Ag(111) substrate to drive a standing-up growth and a bulk-like crystalline phase[47], as the herringbone molecular pairing favors efficient singlet fission kinetics. The upright orientation of the pentacene molecules was verified by means of polarization dependent NEXAFS measurements. To perform the TR-2PPE measurements, the system was pumped with $h\nu_1 = 515\,\text{nm}$ (2.4 eV) and probed with $h\nu_1 = 257\,\text{nm}$ (4.8 eV), with the pulse energies of pump and probe being 20 nJ and 0.05 nJ, respectively. The spot size of the pump beam was approximately $3 \times 10^{-4}\,\text{cm}^2$, corresponding to a pump fluence of $\sim 55\,\mu\text{J/cm}^2$. The repetition rate of the laser was set to 577 kHz and the pulse width to 310 fs. The sample was kept at 200 K during the measurements. A bias of -1.8 V was applied to the sample and the spectra were acquired with a pass energy of 1 eV. Figure 3.2a shows the pseudo-color TR-2PPE map consisting of photoemission spectra acquired as a function of the pump-probe delay. To remove the background due to the 2PPE signal generated from the individual pump and probe pulses we subtracted an

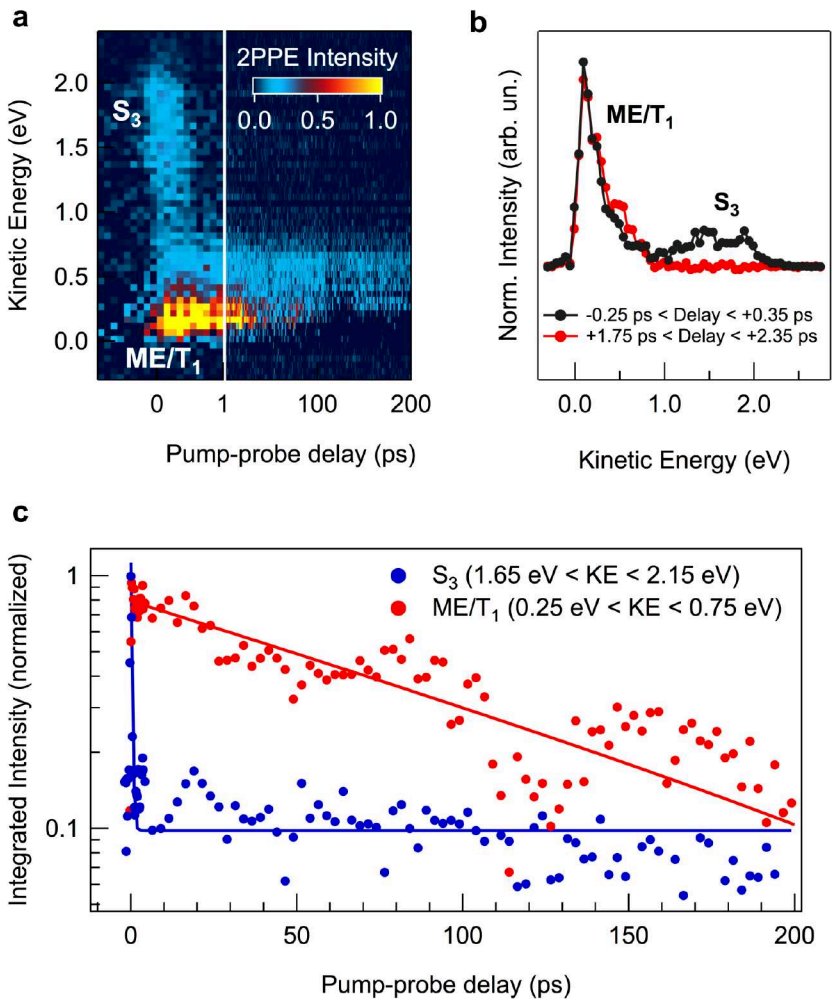


**Figure 3.2 | TR-2PPE analysis. a** Pseudo-color TR-2PPE maps of 2 ML pentacene film in a pump-probe delay range up to 200 ps. Unpumped data have been subtracted to the acquired spectrum at each pump-probe delay. Scale bar represents the normalized 2PPE intensity. **b** Photoemission spectra obtained by integrating the TR-2PPE map in two delay ranges, i.e. at about time zero (black) and at 6 ps (red). The $T_1$ is found at lower kinetic energies, while at $E_k$ higher than 1 eV at short delay times we observe the feature due to the singlet excited states. **c** $T_1$ and $S_3$ decay dynamics, solid lines represent the exponential fitting curves. The lifetimes resulting from the fits are $0.30 \pm 0.02$ ps for $S_3$, and $110 \pm 10$ ps for $T_1$. Error bars represent one standard deviation. Figure adapted from Costantini et al. 1.

average of three spectra taken at negative delay times to the entire map; this procedure is commonly used to separate the pump-induced signal to the time-

independent 2PPE background of the isolated pump and probe pulses. We observe a short-lived state at pump-probe delays below 1 ps that we may assign to $S_3$, as the 515 nm excitation is resonant to the $S_0 \rightarrow S_3$ transition. However, if we integrate the photoemission spectra acquired around time zero (black trace in Figure 3.2b) we may also assume that the broad feature that appears above 1 eV is due to a superposition of $S_3$, the underlying $S_2$ and $S_1$, to which the system promptly relaxes after the excitation. A similar behavior has been reported for tetracene crystals[33]. At lower kinetic energies we observe a long-lived state which extends for more than 100 ps, which we assign to $T_1$ instead. A thorough TR-2PPE characterization of singlet fission in pentacene with a better temporal resolution ($\sim$ 100fs) was already published by Chan et al., who also proved the existence of the intermediate $^1$(TT) state[16]. Since our main interest is in characterizing the triplet excited states in pentacene by means of time-resolved X-ray spectroscopies, TR-2PPE in this case was used as a tool for determining the lifetime of triplet excitons in order to verify the quality of the film and to define the optimal pump fluence to be used.

According to the literature, the $S_0$ HOMO for pentacene lies 5.14 eV below the vacuum level[48], while $S_3$ and $T_1$ are found 2.89 eV and 4.27 eV below the vacuum level, respectively[19,49]. The vacuum level in Figure 3.2 corresponds to the low energy cut-off at $E_k = 0$ eV, therefore, by using probe pulses of 4.8 eV, we expect and measure electrons emitted from the $S_3$ state with a kinetic energy of $\sim$ 1.9 eV and electrons from the triplet state $T_1$ at about 0.5 eV. To evaluate the lifetime of both $S_3$ and $T_1$ the photoemission intensity reported in Figure 3.2a was integrated in high (1.65 eV $< E_k <$ 2.15 eV) and low (0.25 eV $< E_k <$ 0.75 eV) kinetic energy regions, comprising the $S_3$ and $T_1$ states, respectively. The curves are reported in Figure 3.2c, with the solid lines corresponding to the exponential fits. The lifetimes of $S_3$ and $T_1$ that best fit the experimental data are $\tau_{S_3} = 0.30 \pm 0.02$ ps and $\tau_{T_1} = 110 \pm 10$ ps. Chan et al. reported a lifetime of $110 \pm 20$ fs and $\sim$ 250 ps for the singlet and triplet states for a 2 ML film, respectively[16]. In our measurement we are limited in temporal resolution by the laser pulse width of $\sim$ 300 fs, and $\tau_{S_3} = 0.30 \pm 0.02$ ps is actually an indicator of the pump-probe cross-correlation of the setup. For what concerns the triplet states, the shorter lifetime that we detected can be easily related to an incomplete second layer. In films with thickness $\leq$ 2 ML, the escape depth of photoelectrons in TR-2PPE

is high enough to probe the interface with the $C_{60}$ buffer layer, in which the charge transfer becomes a competitive decay channel for triplet excitons. This preliminary characterization of the sample allowed us to optimize the sample growth procedure in order to have an efficient fission yield. Indeed, we observed that, in case of an incomplete $C_{60}$ layer, the poor crystalline structure of the pentacene hinders the triplet formation. Such observation is in agreement with Marciniak et al., who reported a 2% fission yield for microcrystalline pentacene films, due to singlet excimer formation at the abundant trap sites[50]. On the other hand, pentacene films with an adequate quality ensure a clean and unambiguous TR-2PPE signal, which we routinely use for time zero detection when moving to new samples.

## 3.3 The triplet exciton signature in TR-XAS

With the TR-2PPE measurements presented in previous section we established the growth procedure and pump fluence requirements to track pentacene triplet exciton dynamics. Adopting analogous pumping conditions, we probed the carbon K absorption edge, to perform time-resolved X-ray absorption (TR-XAS). The results reported in this section have been published on Communications Physics[1].

We performed our measurements on a 5 ML pentacene film on $C_{60}$/Ag(111). Time-resolved XAS spectra were acquired using 515 nm laser pulses as a pump and probing the system with synchrotron X-ray pulses. To maximize the spatial overlap, the pump beam was set to be $0.5 \times 0.25\,\mathrm{mm}^2$ at the sample, and to have a photon density similar to the one used for TR-2PPE the fluence was increased to $\sim 130\,\mu\mathrm{J/cm}^2$. The TR-XAS signal has been recorded by collecting carbon KVV Auger electrons from both the pumped and unpumped hybrid pulses. A complete description of the experimental procedure can be found in Section 2.3.3. The stroboscopic acquisition that we adopted ensures a proper normalization of the data, hence compensating the X-ray pulse intensity variations due to decay and refilling of the X-ray probe beam in the storage ring. A XAS spectrum is measured at each pump-probe delay step by varying the incoming photon energy via

the beamline monochromator. At first, a static X-ray absorption spectrum was recorded to characterize the sample. The region comprising the first LUMO and LUMO+1 resonances is shown in the inset of Figure 3.3. Due to the lower count rate that is obtained by detecting only the electrons emitted by the hybrid pulses of the storage ring (3 mA ring current as opposed to the 310 mA of the multibunch), in time-resolved measurements we have to acquire a minimum of 4 minutes per point to obtain an acceptable signal-to-noise ratio. As a consequence, we limited the photon energy range to 1.5 eV to perform a single scan in $\sim 2$ hours, including the region 1 eV below the first LUMO resonance in the scan window. The selected window is indicated as a blue dashed box in the inset. Figure 3.3a shows the pumped (P, red) and the unpumped (U, blue) carbon K-edge absorption spectra acquired at the temporal overlap between pump and probe pulses, and the signal is also plotted as the transient absorption (P-U/U) in Figure 3.3b. We observe a clear pump-induced feature around 282.5 eV. Considering that the highest achievable resolution for this measurement is set to $\sim 120$ ps by the synchrotron hybrid pulse width, and that in TR-2PPE measurements $T_1$ is the only contribution that is present at delay times longer than 100 ps, we attribute the pump-induced feature in the TR-XAS spectrum to the triplet state. Instead, the shorter lifetime of singlet excited states calls for much shorter X-ray pulses (< 100 fs) for them to be visible in absorption spectra. Therefore, the optically pumped XAS state that appear at 282.5 eV can be confidently ascribed to C K-edge transitions originating from a fraction of pentacene molecules in the triplet excited state. Given the pump photon density of $\sim 5 \times 10^{17}$ photons/pulse and calculating the number of absorbed photons in the pentacene film by using Beer's law[51], we get to an excitation density of $\sim 1.3 \times 10^{19}$ excitations/cm$^3$. Now, assuming a density of about $10^{21}$ molecules/cm$^3$, we estimate a fraction of 1 - 2% of the probed molecules to be in the excited state. This is consistent with the amplitude of the transient absorption signal in Figure 3.3b, which ranges around 0.05.

The intensity of the triplet state was also monitored as a function of the pump-probe delay. The transient absorption signal was acquired through consecutive TR-XAS scans and integrated in the region between 282.3 and 282.8 eV, using both the hybrid and the single bunch synchrotron operation modes. The two traces are shown in Figure 3.4. The hybrid mode data have been fitted by the

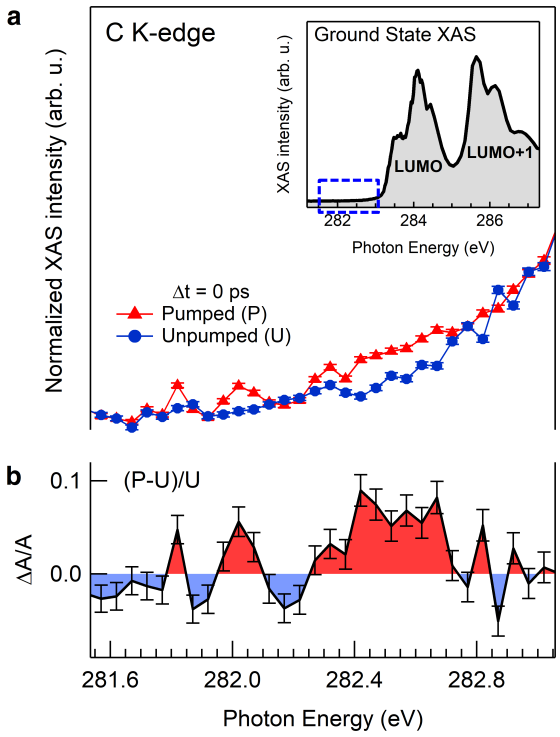


**Figure 3.3 | Time-resolved X-ray absorption on pentacene. a** Pre-edge region of the pentacene Carbon K-edge X-ray absorption spectrum (XAS) with (red) and without (blue) the optical pump at time zero. In the inset an expanded view of the spectra up to the pentacene LUMO+1 is reported. The blue dashed box indicates the acquisition window of the TR-XAS measurement. **b** Transient absorption calculated as ratio (pumped-unpumped)/unpumped. We observe intensity enhancement at about 282.5 eV. Error bars represent one standard deviation. Figure adapted from Costantini et al. [1].

convolution of an exponential decay and a Gaussian function (dashed line). The Gaussian width has been fixed at 120 ps FWHM, the estimated X-ray pulse width. The best fit yields a lifetime of $0.3 \pm 0.2$ ns. The onset in the transient absorption at time zero is better visible in the single bunch measurement, in which the X-ray pulse width is halved ($\sim 60$ ps). As already mentioned in Section 2.3.3, besides the difference in pulse width, data acquired in hybrid mode are partly affected by X-ray induced radiation damage due to the higher photon flux. Sample damage was therefore characterized in detail. As for the laser induced effects, we applied the two-temperature model[52,53] to evaluate the heating of the silver substrate (that we assumed to be comparable to the increment in the film temperature). We estimate a maximum increase of 0.3°C, which should cause negli-

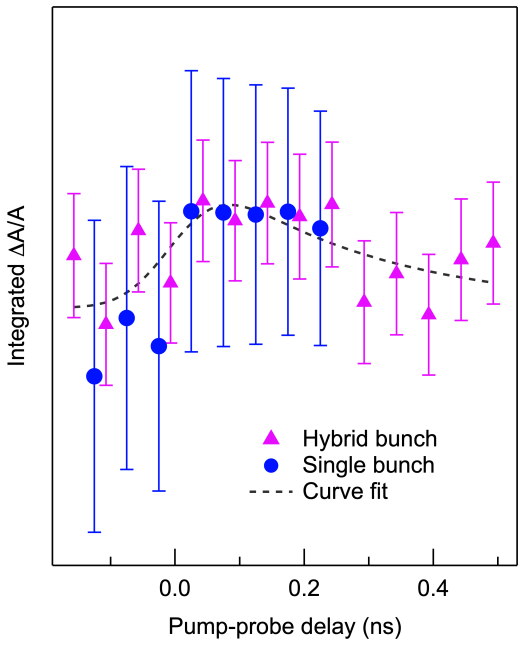


**Figure 3.4 | Triplet state absorption intensity as a function of pump-probe delay.** Two datasets are reported, acquired with two different synchrotron operating modes: hybrid (pink) and single bunch (blue). Error bars represent one standard deviation. The hybrid mode data have been fitted by an exponential decay convoluted with a Gaussian (dashed line). Figure adapted from Costantini et al. [1].

gible broadening effects in the XAS spectra with our experimental resolution. For what concerns X-ray radiation damage, we observed the appearance of a step-like feature in the pre-edge region and the filling of the gap between LUMO and LUMO+1 resonances with increasing exposure to synchrotron radiation. Such behavior has been attributed to the fragmentation of pentacene molecules[54]. To limit radiation damage, the measurement presented in this chapter have been acquired by sampling a fresh spot of the film every 1 - 2 h. Nevertheless, thanks to our acquisition scheme with consecutive pumped and unpumped pulses, control experiments showed that triplet states are visible even in the presence of X-ray damage features.

The experimentally determined $0.3 \pm 0.2$ ns lifetime that we found for the triplet state is well in agreement with previously reported time constants in pentacene multilayers measured via TR-2PPE. Chan et al. reported lifetimes ranging between 250 ps and 400 ps for 2 ML and 10 ML films, respectively[16]. Other tran-

sient absorption studies reported 5 ns triplet lifetimes in polycrystalline pentacene films[55], but it has been shown that film morphology plays a crucial role in determining the decay dynamics[50,56]. In our case, considering the low diffusion rate along the molecular c-axis ($10^{-6}$ cm$^2$/s)[6] and using Fick's law for determining the diffusion length as in Ref 57, we get that it requires $\sim$ 100 ns for triplet excitons in the topmost layer to travel 5 nm and reach the interface with $C_{60}$. This consideration excludes charge transfer to $C_{60}$ from being the preferential decay channel, while it is in agreement with Refs 16, 50 on a relaxation process dominated by exciton trapping on lattice defects.

Further support to the experimental identification of $T_1$ in the TR-XAS is given by ab initio calculations of the core absorption spectra of both the ground state and the triplet excited state, performed by our collaborators at the Technical University of Denmark*. Figure 3.5 shows the simulated spectra of the ground state, $S_0$, and of the $T_1$ valence excited state. Calculations were performed by implementing a core-valence separation (CVS) scheme and optimizing the second order coupled cluster (CC2) using the resolution of identity (RI-) approximation with the aug-cc-pVTZ basis set. Complete details on the theoretical methods can be found in the original paper[1]. The computed X-ray absorption spectra of the two states shown in Figure 3.5 were shifted by -3.2 eV in order to align them to the experimental ground-state spectrum (black curve). It has to be noted that the calculated spectra do not take into account the relative population of $S_0$ and $T_1$ states that we estimated to be 98% and 2%, respectively; on the experimental TR-XAS the intensity of the resonances should therefore scale accordingly. RI-CC2 calculations display a $T_1$ core-excited band located $\sim$ 1.5 eV below the first peak of the LUMO resonance, qualitatively supporting our experimental results.

To summarize, we have here shown that time-resolved X-ray absorption spectroscopy at synchrotrons can be used to measure the dynamics of triplet excited states with chemical selectivity. We characterized a 5 ML film of pentacene, the prototypal singlet fission molecule, by means of picosecond Carbon K-edge XAS. We experimentally identified in the XAS spectrum of optically pumped organic molecules the resonance associated with the fraction of molecules in the triplet excited state. Our assignments are theoretically supported by a novel approach in the state-of-the-art calculations. We established an experimental protocol for

*Group of prof. Sonia Coriani

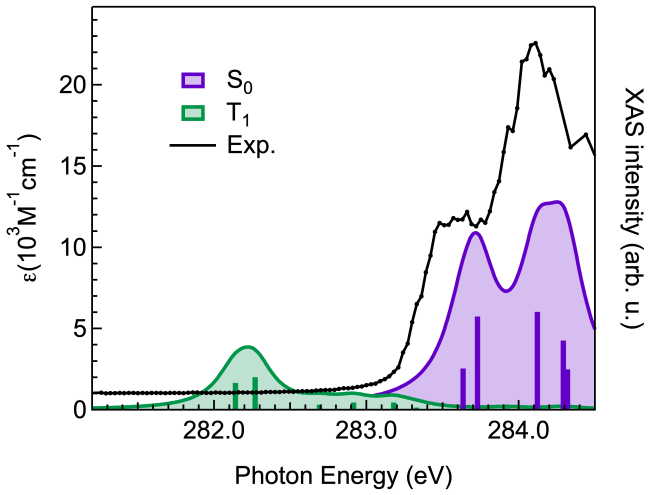


**Figure 3.5 | Calculated X-ray absorption spectra.** Ground state ($S_0$) and triplet excited state ($T_1$) of a single pentacene molecule are shown. Calculations were performed by implementing a core-valence separation (CVS) scheme and optimizing the second order coupled cluster (CC2) using the resolution of identity (RI-) approximation with the aug-cc-pVTZ basis set. Computed spectra were shifted by -3.2 eV to be aligned to the experimental unpumped spectrum (black line). Figure adapted from Costantini et al. [1].

characterizing the long-lived exciton dynamics in singlet fission chromophores with chemical selectivity, which represents a notable advantage over laser-based techniques, for the characterization of heterojunctions and multicomponent architectures. The application of time-resolved X-ray spectroscopies to organic films is still at an early stage, but with a few technical improvements (mainly targeting pulse width and radiation damage) they will represent a useful tool for gathering information about the triplet exciton dynamics in complex structures.

## 3.4 Probing faster exciton dynamics

To observe the faster dynamics of pentacene excitons, we performed TR-XPS experiments at the PG2 beamline at the FLASH free-electron laser[58]. The $\sim$ 100 fs FEL pulses allow us to explore the pico- and sub-picosecond timescales, which are currently inaccessible at synchrotrons. Preliminary measurements for the FLASH beamtime were performed at the T-ReX laboratory at Elettra, a user

facility for time- and angle-resolved photoelectron spectroscopies (TR-ARPES)[59].

### 3.4.1 TR-ARPES at the T-ReX laboratory

At T-ReX a Ti:Sapphire regenerative amplifier delivers ∼ 50 fs pulses at 800 nm with a 250 kHz repetition rate. For our experiment, the second (400 nm) and fourth (200 nm) harmonics of the laser were used to pump and probe a pentacene multilayer grown on a $C_{60}$ covered Au(111) substrate. The acquired photoemission signal is plotted as a function of the pump-probe delay in the pseudo-color map of Figure 3.6. We can clearly distinguish three contributions to the spectrum:

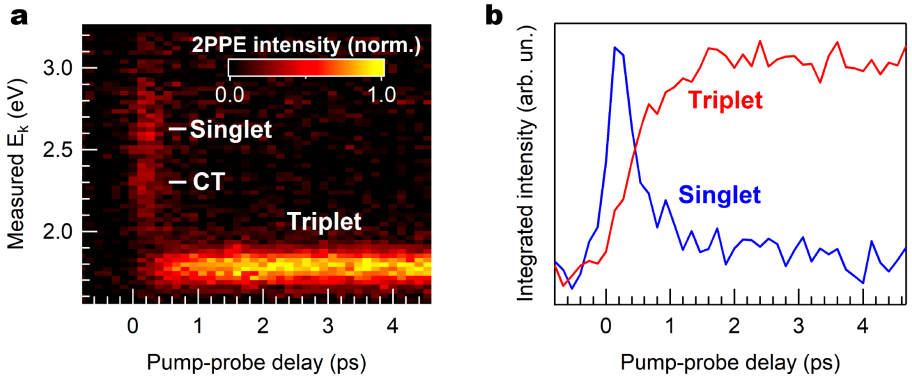


**Figure 3.6 | Singlet fission on pentacene pumped at 400 nm. a** Pseudo-color plot of the photoemission intensity as a function of the pump-probe delay. Triplet exciton are generated despite the off-resonance excitation. **b** Integrated intensities in the singlet (blue) and triplet (red) energy windows. The generation of triplet excitons has a time scale of 600 ± 30 fs.

singlet states, triplet states, and the charge transfer exciton (CT)[16]. The latter is located ∼ 0.95 eV below the vacuum level, it is pumped by the 200 nm pulse and probed by the 400 nm pulse. Despite the off-resonance pump at 400 nm (3.1 eV) triplet excitons are formed on a time scale of 600 ± 30 fs. Nevertheless, the smaller absorption coefficient at 400 nm is responsible for a weaker signal if compared to measurements shown in Figure 3.2, which were performed on-resonance ($S_0 \rightarrow S_3$).

An additional analysis that can be made on the data acquired at T-ReX is on the angular dependence of the photoemission signal. As the detection system is based on a Phoibos 225 electron analyzer coupled with a 2D delay line detec-

tor, ARPES can be performed without rotating the sample by using the angular dispersion modes of the analyzer. The photoemission intensity is therefore acquired as a function of kinetic energy, emission angle and pump-probe delay. In

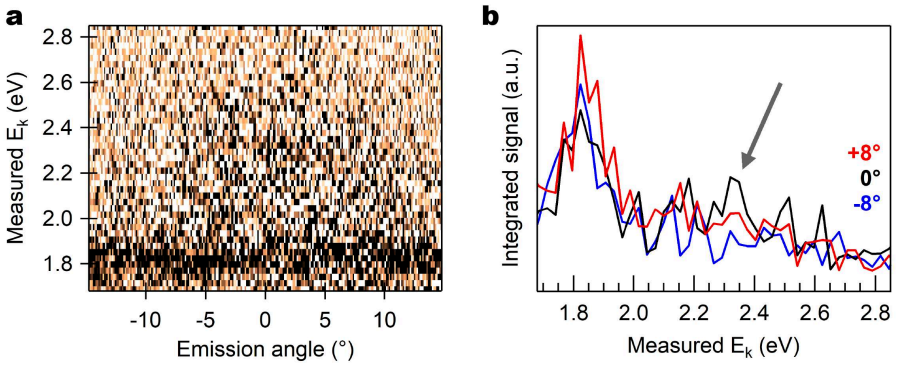


**Figure 3.7 | Angular dependence of triplet and singlet states. a** Photoemission signal integrated for delay times $0 < t < 1.8$ ps as a function of the measured kinetic energy and emission angle. Different behaviors are seen for the triplet and singlet states. **b** Line cuts of the ARPES map along the -8° (blue) 0° (black) and +8° emission angles. The triplet state does not exhibit any angular dependence, while a stronger intensity is found at normal emission in the CT/$S_1$ region.

Figure 3.7a a signal 2D map obtained by integrating the data for delay times between 0 and 1.8 ps is shown. No angular dependence is observed for the $T_1$ state at 1.82 eV, while in the region corresponding to the CT and $S_1$ excitons a slightly higher intensity is found at normal emission, as pointed out by the arrow in Figure 3.7b. This result could be interpreted by considering the calculations performed by Sharifzadeh et al., which predicted the delocalized character of the singlet state in pentacene, as opposed to the triplet state[60]. We plan to repeat the experiment at our laboratory with a pump photon energy resonant to the $S_0 \rightarrow S_1$ transition, in order to have a stronger signal and possibly confirm the angular dependence of the $S_1$ state.

### 3.4.2 TR-XPS at the FLASH FEL: a hint of triplet transfer

FLASH is a self-amplified spontaneous emission (SASE) based FEL, which produces bright coherent pulses with photon energy ranging between 24 and 295 eV

and pulse width around $\sim 30$ - 200 fs[†]. The pulse train is delivered to the users in a set of bunches (up to 8000) with a 1 - 25 µs separation that is repeated at a few Hz[58]. For time-resolved measurements, a Ti:Sapphire laser system mimicking the FLASH pulse train delivers the pump beam, which is made collinear with the FEL before the experimental chamber. Our beamtime was performed at the PG2 beamline, in which the WESPE endstation was mounted[61]. WESPE is equipped with an electron time-of-flight (ToF) spectrometer (THEMIS 1000, SPECS) for measuring photoemission spectra. In order to avoid space charge effects, the FEL intensity was attenuated until an average of 0.5 - 1 electrons per pulse were detected; the temporal overlap between pump and probe pulses was measured on a GaAs crystal prior to the experiment.

In Figure 3.8, a map of the photoemission around the Fermi level as a function

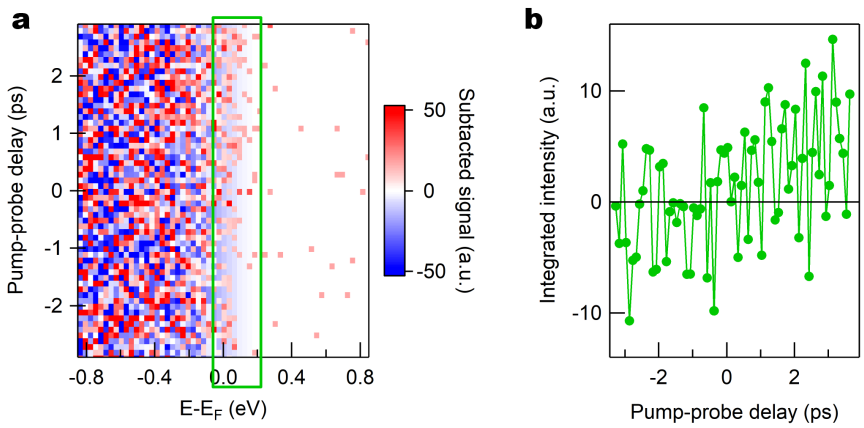


**Figure 3.8 | Valence band probed at 120 eV. a** Pseudo-color map of the photoemission signal as a function of the pump-probe delay. The matrix has been subtracted by smoothed average of the unpumped spectrum. **b** Integrated signal intensity around the Fermi edge (green box in panel a). At time zero the signal increases, compatibly with the generation of triplet excitons.

of the delay between pump (400 nm) and probe (120 eV) is reported, which defined the conditions to measure the triplet excitons in this experimental setup. The map was acquired on a pentacene multilayer ($\sim 5$ ML) grown on a $C_{60}$ covered Ag(111) crystal. The measurement is considerably noisy if compared to the previously reported TR-2PPE spectra, but the integrated signal around the Fermi edge shows a slight increase in the photoemission intensity after time zero, which

[†]Parameters for FLASH1 operation

we relate to the formation of triplet excitons. The poor signal-to-noise ratio in this measurement is reasonably due to a lower cross section for the photoemission from the triplet state at this photon energy, and to the background photoemission signal from ground state molecules, which is not present in TR-2PPE spectra acquired with a probe photon energy below the sample work function.

The photoelectron response as a function of the pump fluence was also investigated by monitoring the C1s core level, which revealed a rather interesting behavior. In Figure 3.9a the spectra taken with a 360 eV probe photon and for $\sim 2.5$ and $\sim 1.3\,\mathrm{mJ/cm^2}$ pump fluences (400 nm) are shown. With high pump fluences the data qualitatively replicate the behavior of a space charge induced shift[58,62], whereas the data acquired with a reduced pump fluence present more complex dynamics. In Figure 3.9b the peak shifts as extracted from the C1s fits are reported. The amplitude of the shifts is referred to the offset obtained from fitting the response at positive delay times with an exponential decay, thus discarding the dynamics that have not fully recovered within the period between consecutive laser pulses ($\sim 1\,\mu s$). Interestingly, the maximum shift at $1.3\,\mathrm{mJ/cm^2}$ is not obtained at time zero, but at $t \approx 6$ ps. Such time scale matches almost perfectly the charge transfer rate of triplet excitons from the pentacene film to the $C_{60}$ measured via TR-2PPE by Chan et al. ($5 \pm 1$ ps)[16] and calculated through time-dependent density functional theory (TDDFT) by Zheng et al. ($\sim 7.7$ ps)[63], suggesting that the kinetic energy shift is related to the dissociation of the triplet excitons at the pentacene/$C_{60}$ interface.

Due to the fact that the escape depth of the photoelectrons at 80 eV allows us to probe mainly the topmost 1 - 2 pentacene layers, we assign the kinetic energy variations to the presence of transient electric fields (long range) rather than to chemical shifts (molecular scale). This would also explain the slow transition observed at negative delays (for both the high and low pump fluence data). To understand such behavior one must get rid of the assumption that the kinetic energy of the photoelectron is fully determined at the time of the photoemission; indeed, for the $\sim 80$ eV electrons that were measured in the dataset reported in Figure 3.9, it required roughly 10 ns to cover the 53 mm distance between the sample and the analyzer. Given the finite flight time, the propagation of the photoelectrons is still subject to perturbation by long range transient fields that are created on the sample by the pump pulse[64,65]. In metals, the photo-excited

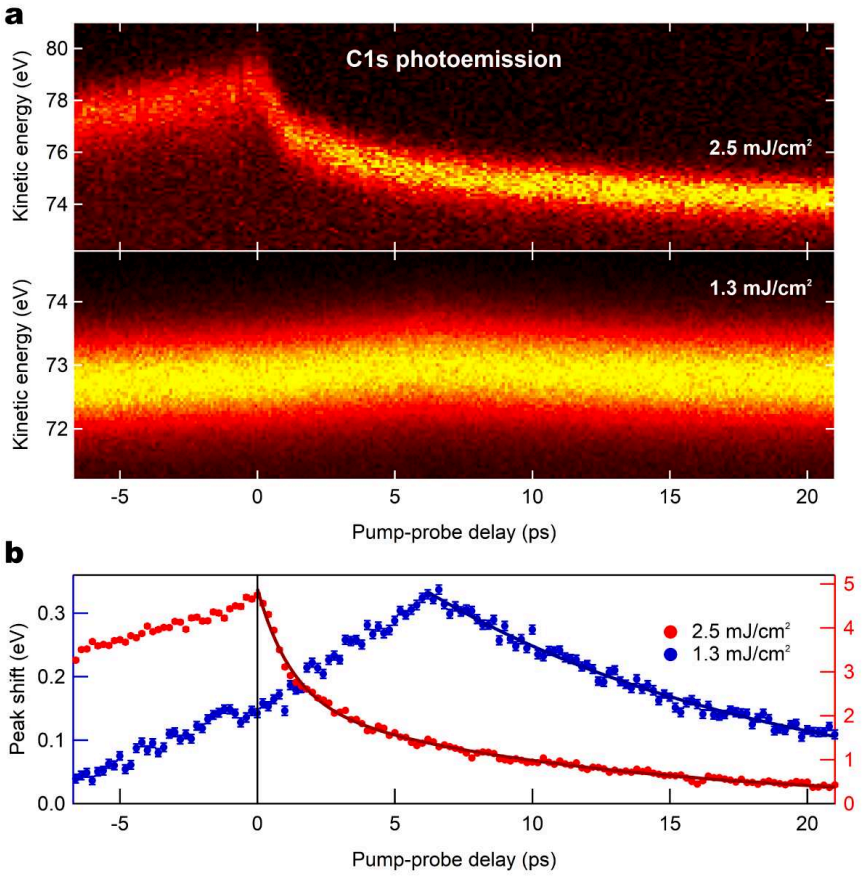


**Figure 3.9 | C1s TR-XPS spectra on pentacene/$C_{60}$. a** Photoelectron response as a function of the pump-probe delay for high (∼ 2.5 mJ/cm$^2$) and low (∼ 1.3 mJ/cm$^2$) pump fluences. At high fluence the kinetic energy shift is ascribable to surface photovoltage and space charge effects in semiconductors, and it is used to determine the temporal overlap between pump and probe pulses. For the low pump fluence the maximum shift is found at t ∼ 6 ps and slow dynamics are found both at positive and negative delay times. **b** Kinetic energy shifts as a function of the pump-probe delay time for the high (red) and low (blue) pump fluence spectra. The peak positions were evaluated from the C1s peak fits. The odd behavior of the low fluence measurement may be related to the triplet exciton dissociation at the pentacene/$C_{60}$ interface. The amplitude of the shifts is referred to the vertical offset extracted from the exponential fits of the photoelectron response at positive delay times.

charge distribution is promptly screened and the perturbation of the traveling photoelectron is negligible, while in systems with a less efficient screening (e.g. semiconductors) field effects become significant. To the best of our knowledge, there is no analytic solution to describe the photoelectron response at negative

delay times, but the characteristic time scale is directly linked to the spatial profile of the transient electric field[64]. As a qualitative and naïve example, if we assume a uniform planar charge density (neglecting border effects and the transient nature of the process) we have that for the $\sim 300$ meV shift detected at 6.2 ps, the carrier density on the sample should be in the order of $10^5$ electrons/cm$^2$. In a more quantitative evaluation, the charge distribution should have lateral dimensions comparable to the beam diameter and could likely be represented by a transient interface dipole rather than a uniformly charged plane, therefore the above estimate can be taken as a lower limit for the charge density needed to account for the measured effects.

The response at positive delays, on the other hand, reflects the actual time scale of the charge rearrangement induced by the laser pulse. The $\sim 6$ ps delay in the photoelectron response and the favorable alignment of the energy levels in the pentacene/$C_{60}$ interface[63] seem to suggest that the triplet exciton dissociation is the main candidate to explain the C1s peak shift. As the spectrum shifts towards higher kinetic energies, we can picture the induced field with a distribution of negative charges (or an interface dipole accordingly oriented). This is in contrast with what we would expect to happen on this system: an electron transfer from pentacene to $C_{60}$[63] followed by its ultra-fast ($< 10$ fs) injection to the silver substrate[66], leaving an excess of positive charges on the pentacene layer close to $C_{60}$. To account for the direction of the shift we may also need to consider the dielectric response of the molecular film to the optically induced charge density at the interface. Stadtmüller et al. analyzed the modification of the energy level alignment in a $C_{60}$ multilayer as a reaction of the molecular environment to the presence of optically generated excitons[67]. Analogous changes in the polarization energy of both pentacene and $C_{60}$ film could cause a charge redistribution at the interface, resulting in an accelerating field for the photoemitted electrons. Theoretical calculations are currently being performed to validate such hypothesis. It remains unclear why no peak shift is observed at 6 ps in TR-2PPE measurements on the same sample. We deem the different photoelectron kinetic energies responsible for such discrepancy; this assumption is supported by studies on space charge effects, in which it was observed that different core levels can shift in different directions, depending on the kinetic energy of the measured photoelectrons[62,68].

Further considerations on the kinetics of triplet transfer to C60 can be made

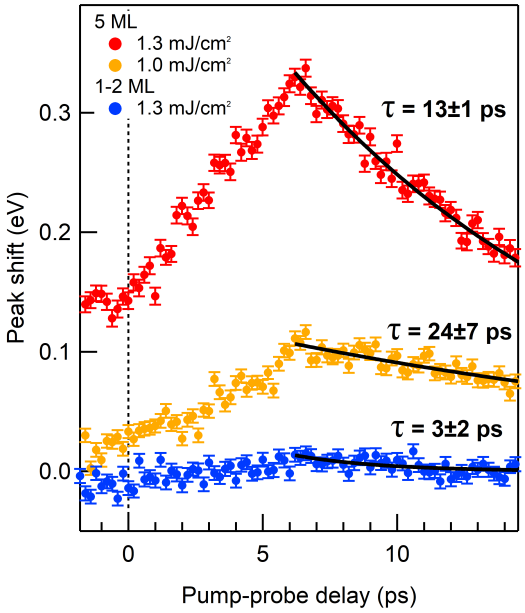


**Figure 3.10 | Thickness and fluence dependence of the C1s shift.** For the 1 - 2 ML film (blue) a small shift with a $3 \pm 2$ ps decay time is detected. Slower decay times are observed on the 5 ML film (orange and red), suggesting the presence of different driving mechanisms in a thicker pentacene crystal. Here, triplet-triplet annihilation may account for the faster decay at higher fluences.

by analyzing the photoelectron response as a function of pump fluence and film thickness, reported in Figure 3.10. First of all, excluding only the measurement performed at 2.5 mJ/cm$^2$ fluence, the maximum peak shift is always found at $\sim$ 6.2 ps. This supports our idea that the observed dynamics is correlated to the transfer of triplet excitons from pentacene to $C_{60}$. Moreover, due to the slow diffusion rate of triplet excitons ($10^{-6}$ cm$^2$/s)[6] we can affirm that the transfer occurs only from the first pentacene layer, since it requires 20 ns to travel 1 nm (i.e. approximately one layer thickness). For this reason, the stronger shifts observed with a 5 ML pentacene film (red and orange dots in Figure 3.10) if compared to the 1 - 2 ML trace (blue dots) cannot be ascribed to a higher number of transferred excitons. Prior studies have shown that, with coverages close to 1 ML, pentacene grows small island of a second molecular layer on top of the incomplete first layer[69]; a reduced interface area between pentacene and $C_{60}$ in the 1 - 2 ML film with respect to the 5 ML film may possibly explain the observed difference

in the shift magnitudes. The decay times are also significantly different in the two samples, with $3 \pm 2$ ps and $13 \pm 1$ ps for the 1 - 2 ML and 5 ML, respectively. We speculate that the time scale in the 1 - 2 ML film is directly determined by the lifetime of the transient interface dipole, while to account for the longer decay times for the 5 ML sample we must also consider a stronger contribution from the dielectric response of the whole crystal. Finally, the decrease in the decay time as a function of the increasing pump fluence that we observed for the 5 ML film can be related to triplet-triplet annihilation processes. Indeed, in a pentacene derivative, fluences higher than 20 $\mu J/cm^2$ were proven to cause a strong damping of the triplet lifetime [70], due to the higher probability of interactions between triplet excitons that result in a radiative recombination process.
As it may have emerged from the text, building a model for this dataset is a non-trivial task, and we hope that theoretical simulations will help interpreting our results. Nevertheless, despite the many open questions, we have shown a strong spectroscopic evidence for triplet transfer in time-resolved XPS, thus expanding the toolbox for the characterization of exciton dynamics in molecular films. Tunable, high repetition rate X-ray sources are the best options for this technique in terms of count rate and probe space charge limitations; to this extent, the planned developments to push the temporal resolution of synchrotron facilities down to the picosecond range would be beneficial to the characterization of the 1 - 10 ps triplet exciton transfer dynamics in organic interfaces.

# References

1. Costantini, R.; Faber, R.; Cossaro, A.; Floreano, L.; Verdini, A.; Hättig, C.; Morgante, A.; Coriani, S.; Dell'Angela, M. Picosecond timescale tracking of pentacene triplet excitons with chemical sensitivity. *Communications Physics* **2019**, *2*, 56.

2. Singh, S.; Jones, W. J.; Siebrand, W.; Stoicheff, B. P.; Schneider, W. G. Laser generation of excitons and fluorescence in anthracene crystals. *The Journal of Chemical Physics* **1965**, *42*, 330–342.

3. Dexter, D. Two ideas on energy transfer phenomena: Ion-pair effects involving the OH stretching mode, and sensitization of photovoltaic cells. *Journal of Luminescence* **1979**, *18-19*, 779–784.

4. Hanna, M. C.; Nozik, A. J. Solar conversion efficiency of photovoltaic and photoelectrolysis cells with carrier multiplication absorbers. *Journal of Applied Physics* **2006**, *100*, 074510.

5. Shockley, W.; Queisser, H. J. Detailed balance limit of efficiency of p-n junction solar cells. *Journal of Applied Physics* **1961**, *32*, 510–519.

6. Smith, M. B.; Michl, J. Singlet Fission. *Chemical Reviews* **2010**, *110*, 6891–6936.

7. Smith, M. B.; Michl, J. Recent Advances in Singlet Fission. *Annual Review of Physical Chemistry* **2013**, *64*, 361–386.

8. Miyata, K.; Conrad-Burton, F. S.; Geyer, F. L.; Zhu, X.-Y. Triplet Pair States in Singlet Fission. *Chemical Reviews* **2019**, *119*, 4261–4292.

9. Monahan, N.; Zhu, X.-Y. Charge Transfer–Mediated Singlet Fission. *Annual Review of Physical Chemistry* **2015**, *66*, 601–618.

10. Zhu, T.; Huang, L. Exciton Transport in Singlet Fission Materials: A New Hare and Tortoise Story. *The Journal of Physical Chemistry Letters* **2018**, *9*, 6502–6510.

11. Kim, H.; Zimmerman, P. M. Coupled double triplet state in singlet fission. *Physical Chemistry Chemical Physics* **2018**, *20*, 30083–30094.

12. Casanova, D. Theoretical Modeling of Singlet Fission. *Chemical Reviews* **2018**, *118*, 7164–7207.

13. Merrifield, R. E. Theory of Magnetic Field Effects on the Mutual Annihilation of Triplet Excitons. *The Journal of Chemical Physics* **1968**, *48*, 4318–4319.

14. Johnson, R. C.; Merrifield, R. E. Effects of Magnetic Fields on the Mutual Annihilation of Triplet Excitons in Anthracene Crystals. *Physical Review B* **1970**, *1*, 896–902.

15. Suna, A. Kinematics of Exciton-Exciton Annihilation in Molecular Crystals. *Physical Review B* **1970**, *1*, 1716–1739.

16. Chan, W.-L.; Ligges, M.; Jailaubekov, A.; Kaake, L.; Miaja-Avila, L.; Zhu, X.-Y. Observing the Multiexciton State in Singlet Fission and Ensuing Ultrafast Multielectron Transfer. *Science* **2011**, *334*, 1541–1545.

17. Pensack, R. D.; Ostroumov, E. E.; Tilley, A. J.; Mazza, S.; Grieco, C.; Thorley, K. J.; Asbury, J. B.; Seferos, D. S.; Anthony, J. E.; Scholes, G. D. Observation of Two Triplet-Pair Intermediates in Singlet Exciton Fission. *Journal of Physical Chemistry Letters* **2016**, *7*, 2370–2375.

18. Zimmerman, P. M.; Zhang, Z.; Musgrave, C. B. Singlet fission in pentacene through multi-exciton quantum states. *Nature Chemistry* **2010**, *2*, 648–652.

19. Zimmerman, P. M.; Bell, F.; Casanova, D.; Head-Gordon, M. Mechanism for singlet fission in pentacene and tetracene: From single exciton to two triplets. *Journal of the American Chemical Society* **2011**, *133*, 19944–19952.

20. Broch, K.; Dieterle, J.; Branchi, F.; Hestand, N. J.; Olivier, Y.; Tamura, H.; Cruz, C.; Nichols, V. M.; Hinderhofer, A.; Beljonne, D.; Spano, F. C.; Cerullo, G.; Bardeen, C. J.; Schreiber, F. Robust singlet fission in pentacene thin films with tuned charge transfer interactions. *Nature Communications* **2018**, *9*.

21. Zirzlmeier, J.; Lehnherr, D.; Coto, P. B.; Chernick, E. T.; Casillas, R.; Basel, B. S.; Thoss, M.; Tykwinski, R. R.; Guldi, D. M. Singlet fission in pentacene dimers. *Proceedings of the National Academy of Sciences* **2015**, *112*, 5325–5330.

22. Yost, S. R. et al. A transferable model for singlet-fission kinetics. *Nature Chemistry* **2014**, *6*, 492–497.

23. Alagna, N.; Han, J.; Wollscheid, N.; Luis Perez Lustres, J.; Herz, J.; Hahn, S.; Koser, S.; Paulus, F.; H. F. Bunz, U.; Dreuw, A.; Buckup, T.; Motzkus, M. Tailoring Ultrafast Singlet Fission by the Chemical Modification of Phenazinothiadiazoles. *Journal of the American Chemical Society* **2019**, *141*, 8834–8845.

24. Eaton, S. W.; Shoer, L. E.; Karlen, S. D.; Dyar, S. M.; Margulies, E. A.; Veldkamp, B. S.; Ramanan, C.; Hartzler, D. A.; Savikhin, S.; Marks, T. J.; Wasielewski, M. R. Singlet Exciton Fission in Polycrystalline Thin Films of a Slip-Stacked Perylenediimide. *Journal of the American Chemical Society* **2013**, *135*, 14701–14712.

25. Busby, E.; Xia, J.; Wu, Q.; Low, J. Z.; Song, R.; Miller, J. R.; Zhu, X.-y.; Campos, L. M.; Sfeir, M. Y. A design strategy for intramolecular singlet fission mediated by charge-transfer states in donor–acceptor organic materials. *Nature Materials* **2015**, *14*, 426–433.

26. Margulies, E. A.; Miller, C. E.; Wu, Y.; Ma, L.; Schatz, G. C.; Young, R. M.; Wasielewski, M. R. Enabling singlet fission by controlling intramolecular charge transfer in $\pi$-stacked covalent terrylenediimide dimers. *Nature Chemistry* **2016**, *8*, 1120–1125.

27. Trinh, M. T.; Pinkard, A.; Pun, A. B.; Sanders, S. N.; Kumarasamy, E.; Sfeir, M. Y.; Campos, L. M.; Roy, X.; Zhu, X.-Y. Distinct properties of the triplet pair state from singlet fission. *Science Advances* **2017**, *3*, e1700241.

28. Conrad-Burton, F. S.; Liu, T.; Geyer, F.; Costantini, R.; Schlaus, A. P.; Spencer, M. S.; Wang, J.; Sánchez, R. H.; Zhang, B.; Xu, Q.; Steigerwald, M. L.; Xiao, S.; Li, H.; Nuckolls, C. P.; Zhu, X. Controlling Singlet Fission by Molecular Contortion. *Journal of the American Chemical Society* **2019**, *141*, 13143–13147.

29. Yost, S. R.; Hontz, E.; Yeganeh, S.; Van Voorhis, T. Triplet vs Singlet Energy Transfer in Organic Semiconductors: The Tortoise and the Hare. *The Journal of Physical Chemistry C* **2012**, *116*, 17369–17377.

30. Congreve, D. N.; Lee, J.; Thompson, N. J.; Hontz, E.; Yost, S. R.; Reusswig, P. D.; Bahlke, M. E.; Reineke, S.; Van Voorhis, T.; Baldo, M. A. External Quantum Efficiency Above 100% in a Singlet-Exciton-Fission-Based Organic Photovoltaic Cell. *Science* **2013**, *340*, 334–337.

31. Wan, Y.; Guo, Z.; Zhu, T.; Yan, S.; Johnson, J.; Huang, L. Cooperative singlet and triplet exciton transport in tetracene crystals visualized by ultrafast microscopy. *Nature Chemistry* **2015**, *7*, 785–792.

32. Zhu, T.; Wan, Y.; Guo, Z.; Johnson, J.; Huang, L. Two Birds with One Stone: Tailoring Singlet Fission for Both Triplet Yield and Exciton Diffusion Length. *Advanced Materials* **2016**, *28*, 7539–7547.

33. Chan, W.-L.; Ligges, M.; Zhu, X.-Y. The energy barrier in singlet fission can be overcome through coherent coupling and entropic gain. *Nature Chemistry* **2012**, *4*, 840–845.

34. Ito, S.; Nagami, T.; Nakano, M. Molecular design for efficient singlet fission. *Journal of Photochemistry and Photobiology C: Photochemistry Reviews* **2018**, *34*, 85–120.

35. Papadopoulos, I.; Zirzlmeier, J.; Hetzer, C.; J. Bae, Y.; D. Krzyaniak, M.; R. Wasielewski, M.; Clark, T.; R. Tykwinski, R.; M. Guldi, D. Varying the Interpentacene Electronic Coupling to Tune Singlet Fission. *Journal of the American Chemical Society* **2019**, *141*, 6191–6203.

36. Arias, D. H.; Ryerson, J. L.; Cook, J. D.; Damrauer, N. H.; Johnson, J. C. Polymorphism influences singlet fission rates in tetracene thin films. *Chemical Science* **2016**, *7*, 1185–1191.

37. Pace, N. A.; Arias, D. H.; Granger, D. B.; Christensen, S.; Anthony, J. E.; Johnson, J. C. Dynamics of singlet fission and electron injection in self-assembled acene monolayers on titanium dioxide. *Chemical Science* **2018**, *9*, 3004–3013.

38. Schrauben, J. N.; Zhao, Y.; Mercado, C.; Dron, P. I.; Ryerson, J. L.; Michl, J.; Zhu, K.; Johnson, J. C. Photocurrent Enhanced by Singlet Fission in a Dye-Sensitized Solar Cell. *ACS Applied Materials & Interfaces* **2015**, *7*, 2286–2293.

39. Kunzmann, A.; Gruber, M.; Casillas, R.; Zirzlmeier, J.; Stanzel, M.; Peukert, W.; Tykwinski, R. R.; Guldi, D. M. Singlet Fission for Photovoltaics with 130% Injection Efficiency. *Angewandte Chemie International Edition* **2018**, *57*, 10742–10747.

40. Thompson, N. J.; Wilson, M. W. B.; Congreve, D. N.; Brown, P. R.; Scherer, J. M.; Bischof, T. S.; Wu, M.; Geva, N.; Welborn, M.; Voorhis, T. V.; Bulović, V.; Bawendi, M. G.; Baldo, M. A. Energy harvesting of non-emissive triplet excitons in tetracene by emissive PbS nanocrystals. *Nature Materials* **2014**, *13*, 1039–1043.

41. Kroupa, D. M.; Arias, D. H.; Blackburn, J. L.; Carroll, G. M.; Granger, D. B.; Anthony, J. E.; Beard, M. C.; Johnson, J. C. Control of Energy Flow Dynamics between Tetracene Ligands and PbS Quantum Dots by Size Tuning and Ligand Coverage. *Nano Letters* **2018**, *18*, 865–873.

42. Ehrler, B.; Wilson, M. W.; Rao, A.; Friend, R. H.; Greenham, N. C. Singlet exciton fission-sensitized infrared quantum dot solar cells. *Nano Letters* **2012**, *12*, 1053–1057.

43. Jadhav, P. J.; Mohanty, A.; Sussman, J.; Lee, J.; Baldo, M. A. Singlet Exciton Fission in Nanostructured Organic Solar Cells. *Nano Letters* **2011**, *11*, 1495–1498.

44. Willems, R. E. M.; Meskers, S. C. J.; Wienk, M. M.; Janssen, R. A. J. Effect of Charge-Transfer State Energy on Charge Generation Efficiency via Singlet Fission in Pentacene–Fullerene Solar Cells. *The Journal of Physical Chemistry C* **2019**, *123*, 10253–10261.

45. Lin, Y. L.; Zhang, F.; Kerner, R. A.; Yang, T. C.-J.; Kahn, A.; Rand, B. P. Variable charge transfer state energies at nanostructured pentacene/$C_{60}$ interfaces. *Applied Physics Letters* **2018**, *112*, 213302.

46. Lin, Y. L.; Fusella, M. A.; Kozlov, O. V.; Lin, X.; Kahn, A.; Pshenichnikov, M. S.; Rand, B. P. Morphological Tuning of the Energetics in Singlet Fission Organic Solar Cells. *Advanced Functional Materials* **2016**, *26*, 6489–6494.

47. Dougherty, D. B.; Jin, W.; Cullen, W. G.; Reutt-Robey, J. E.; Robey, S. W. Striped domains at the pentacene:$C_{60}$ interface. *Applied Physics Letters* **2009**, *94*, 023103.

48. Kakuta, H.; Hirahara, T.; Matsuda, I.; Nagao, T.; Hasegawa, S.; Ueno, N.; Sakamoto, K. Electronic structures of the highest occupied molecular orbital bands of a pentacene ultrathin film. *Physical Review Letters* **2007**, *98*, 247601.

49. Breeze, J.; Tan, K.-J.; Richards, B.; Sathian, J.; Oxborrow, M.; Alford, N. M. Enhanced magnetic Purcell effect in room-temperature masers. *Nature Communications* **2015**, *6*, 6215.

50. Marciniak, H.; Fiebig, M.; Huth, M.; Schiefer, S.; Nickel, B.; Selmaier, F.; Lochbrunner, S. Ultrafast Exciton Relaxation in Microcrystalline Pentacene Films. *Physical Review Letters* **2007**, *99*, 176402.

51. Swinehart, D. F. The Beer-Lambert Law. *Journal of Chemical Education* **1962**, *39*, 333.

52. Anisimov, S. I.; Kapeliovich, B. L.; Perel'man, T. L. Electron emission from metal surfaces exposed to ultrashort laser pulses. *Soviet Physics - JETP* **1974**, *39*, 375–377.

53. Dell'Angela, M.; Hieke, F.; Sorgenfrei, F.; Gerken, N.; Beye, M.; Gerasimova, N.; Redlin, H.; Wurth, W. Ultrafast surface dynamics probed with time resolved photoemission. *Surface Science* **2016**, *643*, 197–202.

54. Zheng, F.; Park, B.-N.; Seo, S.; Evans, P. G.; Himpsel, F. J. Orientation of pentacene molecules on SiO2: From a monolayer to the bulk. *The Journal of Chemical Physics* **2007**, *126*, 154702.

55. Rao, A.; Wilson, M. W. B.; Hodgkiss, J. M.; Albert-Seifried, S.; Bässler, H.; Friend, R. H. Exciton Fission and Charge Generation via Triplet Excitons in Pentacene/$C_{60}$ Bilayers. *Journal of the American Chemical Society* **2010**, *132*, 12698–12703.

56. Burdett, J. J.; Müller, A. M.; Gosztola, D.; Bardeen, C. J. Excited state dynamics in solid and monomeric tetracene: The roles of superradiance and exciton fission. *The Journal of Chemical Physics* **2010**, *133*, 144506.

57. Akselrod, G. M.; Deotare, P. B.; Thompson, N. J.; Lee, J.; Tisdale, W. A.; Baldo, M. A.; Menon, V. M.; Bulović, V. Visualization of exciton transport in ordered and disordered molecular solids. *Nature Communications* **2014**, *5*, 3646.

58. Hellmann, S.; Sohrt, C.; Beye, M.; Rohwer, T.; Sorgenfrei, F.; Marczynski-Bühlow, M.; Kalläne, M.; Redlin, H.; Hennies, F.; Bauer, M.; Föhlisch, A.; Kipp, L.; Wurth, W.; Rossnagel, K. Time-resolved x-ray photoelectron spectroscopy at FLASH. *New Journal of Physics* **2012**, *14*, 013062.

59. Cilento, F.; Crepaldi, A.; Manzoni, G.; Sterzi, A.; Zacchigna, M.; Bugnon, P.; Berger, H.; Parmigiani, F. Advancing non-equilibrium ARPES experiments by a 9.3 eV coherent ultrafast photon source. *Journal of Electron Spectroscopy and Related Phenomena* **2016**, *207*, 7–13.

60. Sharifzadeh, S.; Darancet, P.; Kronik, L.; B. Neaton, J. Low-Energy Charge-Transfer Excitons in Organic Solids from First-Principles: The Case of Pentacene. *The Journal of Physical Chemistry Letters* **2013**, *4*, 2197–2201.

61. Mercurio, G.; Makhotkin, I. A.; Milov, I.; Kim, Y. Y.; Zaluzhnyy, I. A.; Dziarzhytski, S.; Wenthaus, L.; Vartanyants, I. A.; Wurth, W. Surface structure determination by x-ray standing waves at a free-electron laser. *New Journal of Physics* **2019**, *21*, 033031.

62. Dell'Angela, M. et al. Vacuum space charge effects in sub-picosecond soft X-ray photoemission on a molecular adsorbate layer. *Structural Dynamics* **2015**, *2*.

63. Zheng, Z.; Tummala, N. R.; Fu, Y. T.; Coropceanu, V.; Brédas, J. L. Charge-Transfer States in Organic Solar Cells: Understanding the Impact of Polarization, Delocalization, and Disorder. *ACS Applied Materials and Interfaces* **2017**, *9*, 18095–18102.

64. Yang, S.-L.; Sobota, J. A.; Kirchmann, P. S.; Shen, Z.-X. Electron propagation from a photo-excited surface: implications for time-resolved photoemission. *Applied Physics A* **2014**, *116*, 85–90.

65. Widdra, W.; Bröcker, D.; Gießel, T.; Hertel, I.; Krüger, W.; Liero, A.; Noack, F.; Petrov, V.; Pop, D.; Schmidt, P.; Weber, R.; Will, I.; Winter, B. Time-resolved core level photoemission: surface photovoltage dynamics of the SiO2/Si(1 0 0) interface. *Surface Science* **2003**, *543*, 87–94.

66. Gibson, A. J.; Temperton, R. H.; Handrup, K.; O'Shea, J. N. Resonant core spectroscopies of the charge transfer interactions between $C_{60}$ and the surfaces of Au(111), Ag(111), Cu(111) and Pt(111). *Surface Science* **2017**, *657*, 69–78.

67. Stadtmüller, B.; Emmerich, S.; Jungkenn, D.; Haag, N.; Rollinger, M.; Eich, S.; Maniraj, M.; Aeschlimann, M.; Cinchetti, M.; Mathias, S. Strong modification of the transport level alignment in organic materials after optical excitation. *Nature Communications* **2019**, *10*, 1470.

68. Kühn, D.; Giangrisostomi, E.; Jay, R. M.; Sorgenfrei, F.; Föhlisch, A. The influence of x-ray pulse length on space-charge effects in optical pump/x-ray probe photoemission. *New Journal of Physics* **2019**, *21*, 073042.

69. Meyer zu Heringdorf, F.-J.; Reuter, M. C.; Tromp, R. M. Growth dynamics of pentacene thin films. *Nature* **2001**, *412*, 517–520.

70. Pensack, R. D.; Grieco, C.; Purdum, G. E.; Mazza, S. M.; Tilley, A. J.; Ostroumov, E. E.; Seferos, D. S.; Loo, Y.-L.; Asbury, J. B.; Anthony, J. E.; Scholes, G. D. Solution-processable, crystalline material for quantitative singlet fission. *Materials Horizons* **2017**, *4*, 915–923.

# 4 Observing the triplet exciton transfer

After having characterized the triplet exciton dynamics in pentacene by means of time-resolved X-ray spectroscopies, we investigated the interface between a singlet fission chromophore and an organic acceptor.

## 4.1 Singlet fission in photovoltaics: tetracene on Cu phthalocyanine

A possible implementation of singlet fission for multi-exciton generation in photovoltaic devices has been widely investigated over the last decade, with pioneering research led by the group of Marc Baldo at the Massachusetts Institute of Technology[1–5]. Their work highlighted the main limits of this technology as well as the design guidelines to overcome them, and proved the possibility of breaking the barrier of 100% in external quantum efficiency[2,3](i.e. the fraction of incident photons that are converted into electrons and collected on the metallic contacts). The issue of triplet exciton extraction, which has already been discussed in the previous chapter, represents the current bottleneck for the promised gains in power conversion efficiencies of light harvesting devices. Furthermore, it has been observed that the effective gap, i.e. the energy difference between the HOMO of the donor and the LUMO of the acceptor, directly determines the open circuit voltage of the device[6,7], which is linearly correlated to the power conversion efficiency. If the acceptor is chosen to ensure a resonant transfer from triplet states, which have roughly half the energy of singlet states, the open circuit voltage is reduced by a factor of two, therefore cancelling any net

gain introduced by the exciton multiplication. Triplets are also dark states, meaning that optical absorption in the region between triplet and singlet excitons is spin forbidden; this fact limits the available portion of the solar spectrum, and precludes the goal of obtaining power conversion efficiencies over the Shockley-Queisser limit[8] with devices based on an individual singlet fission chromophore[9]. For this reason it is beneficial to couple the fission material with a long wavelength absorber, in order to cover a broader portion of the solar spectrum. To this aim, the most studied molecule is tetracene, which has been interfaced both to copper phthalocyanine[1,10] and to silicon[5,11].

Tetracene (Tc) absorbs at $\lambda < 550$ nm, undergoes singlet fission in the 10 - 100 ps time scale[12–14] and, as a result of the interplay between singlet fission and triplet fusion, has an exciton diffusion length of $\sim 300$ nm[15–17]. Copper phthalocyanine (CuPc) has a complementary optical absorption spectrum and may act as an acceptor for the Tc triplet excitons, making the Tc/CuPc junction a valid prototype of singlet fission solar cell. A first device based on the Tc/CuPc/$C_{60}$ structure was proposed in 2011, showing that the presence of CuPc was leading to an increased photocurrent[1]. More recently, Tc was used as a sensitizer in a silicon solar cell, demonstrating efficient triplet exciton transfer to the semiconductor[5]. Despite the promising results, however, the overall efficiency of prototypal singlet fission devices is not yet competitive with the 15 - 20% offered by commercially available solar cells, and further work is needed to tackle the technological challenges. In particular, to overcome the poor carrier collection it is crucial to characterize and properly tailor the electronic properties of the interfaces between singlet fission chromophores and the acceptor materials.

Following the lead of Tritsch et al.[10], we select the tetracene and copper phthalocyanine heterojunction as a model system for triplet transfer. In the above cited paper, the authors characterized the CuPc/Tc interface on a CuPc/Tc/$C_{60}$ /Au(111) junction and observed an efficient triplet transfer from Tc to CuPc. We used the multiple spectroscopies available at the ANCHOR-SUNDYN endstation to characterize in detail the interface between tetracene and copper phthalocyanine. In particular, we investigated how the morphology of the interface, in terms of the mutual orientation between the molecules of the two species, affects the electronic dynamics of the system. We obtained two morphologically different interfaces by reversing the deposition order of CuPc and Tc species,

as evidenced by NEXAFS characterization presented in Appendix A. For both cases, we first determined the energy level alignment of both occupied valence states and unoccupied excited states, by combining UPS with TR-2PPE data. We then performed pump-probe XPS, exploiting the wavelength tunability of our pump beam to selectively excite the two chromophores. C1s core levels revealed spectral shifts that are interpreted as a proof of the transient electric field that is created at the interface upon exciton transfer.

### 4.1.1 Energy level alignment

The seemingly trivial task of drawing the energy level alignment in organic interfaces has been a matter of debate in the recent literature[18–22]. In the design of novel devices, the choice of materials traditionally relied on the assumption that the vacuum level remains constant through the whole structure, but numerous reports showed that such assumption does not universally apply[23–28]. Energy diagrams modeled with a bottom-up approach from the isolated materials may therefore result misleading, and the complete system has to be characterized for drawing a more accurate scheme. In particular, the presence of the metallic substrate, which represents the electrode in prototypal devices, has a key role in determining the electronic equilibrium of the whole heterostructure and cannot be neglected. For this reason, we have referred all measurements to the Fermi level of the metal.

We examine here two different samples, with Tc and CuPc grown in alternate order on a Ag(111) crystal, with the aim of determining the energy level alignment. First, we thermally evaporated Tc on the Ag(111) substrate at 230 K; under these conditions the flat $\alpha$-phase monolayer is achieved[29], while the multilayer is seen to form crystallites with a large height-to-width ratio covering only a small fraction of the surface[30,31]. CuPc was then deposited on top of Tc until the UPS spectra showed no changes, to have a minimum of 2 nm thick overlayer[10]. In a separate moment, the sample growth was also monitored by polarization dependent NEXAFS, as shown in Appendix A; the Tc film was seen to be predominantly flat, in agreement with the literature, while the non-perfect dichroism in the N K-edge spectra points to a slightly tilted orientation of the CuPc molecules. The cartoon in Figure 4.1b qualitatively represents the sample morphology. To char-

acterize the frontier orbitals, HOMOs and LUMOs, we performed both UPS and TR-2PPE, which are shown jointly in Figure 4.1a. TR-2PPE was measured on the full CuPc/Tc/Ag(111) sample using 515 and 626 nm (2.41 and 1.98 eV) pulses to selectively pump Tc and CuPc molecules, respectively, and 257 nm (4.82 eV) pulses as a probe. A - 3.0 V bias was applied to the isolated sample to enhance the detection of the low kinetic energy electrons. The TR-2PPE spectra were aligned to the Fermi energy of the substrate by adding the sample work function and subtracting the probe photon energy and the bias to the measured photoelectron kinetic energy. Different cuts of the TR-2PPE maps are shown in Figure 4.1a, for delays - 0.25 < t < 0.25 ps (solid black lines) and 4.75 < t < 5.25 ps (dashed black lines) to identify singlet and triplet excited states. In Figure 4.1c we draw a naïve energy level scheme for the heterojunction, in which the colored boxes represent the peak positions in UPS and TR-2PPE spectra. Other authors suggest to use the onsets rather than the peak maxima for reference[32] as such method gives a more accurate determination of the optical gap, but we choose to select the peak-to-peak distance as it yields the energy of the more probable $S_0 \rightarrow S_1$ transition, corresponding to an absorption maximum.

Notably, by referring all the spectra to the substrate Fermi level, the unoccupied $S_1$ state of CuPc is found below zero. Ideally, this means that electrons from the Ag surface could populate such state, but as no signal is found in the corresponding region of the UPS spectrum, it has to be inferred that $S_1$ remains unoccupied despite its energy position. To properly discuss the alignment scheme in Figure 4.1c, we have to distinguish between transport and optical gap: the former refers to the energy needed to form two independent charge carriers (electron and hole) in the molecular solid, while the latter refers to the energy required to create an exciton, the bound electron-hole pair; the energy difference between the two is, by definition, the exciton binding energy[33,34]. With TR-2PPE we are actually probing the electrons that are in an excitonic state, bound to a hole in the HOMO, and therefore we are underestimating the position of the unbound $S_1$ state by at most the exciton binding energy, which is in the order of 0.1 - 1 eV in organic semiconductors[35–37]. This aspect may in fact lead to ambiguities in the energy level alignment provided in Figure 4.1, as we are combining the hole transport levels measured by UPS with the exciton levels probed by TR-2PPE, and thus we can only use it as a qualitative estimate of the driving forces for the

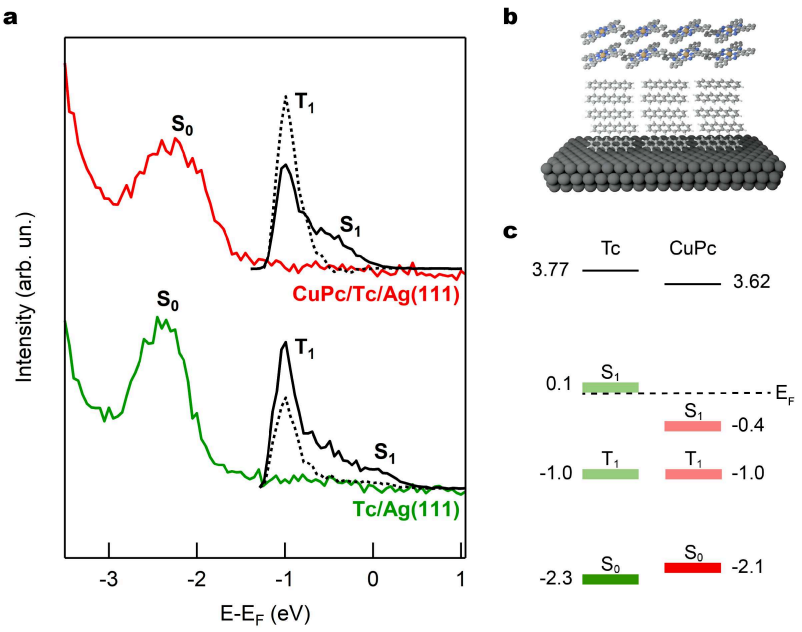


**Figure 4.1 | Energy levels of CuPc/Tc/Ag(111). a** UPS spectra for Tc/Ag(111) (green) and for CuPc/Tc/Ag(111) (red). TR-2PPE spectra acquired around time zero (solid black lines) and at 5ps delay (dashed black line) on the complete interface are overlaid to the photoemission spectra. To selectively excite Tc and CuPc, we used 515 and 626 nm pump photon energies, respectively. **b** Illustration of the interface morphology determined by polarization dependent NEXAFS. **c** Energy level alignment. Colored boxes represent the peak positions identified in panel **a**, black bars are the vacuum levels. All values are given in eV.

exciton transfer through the interface. A more detailed analysis would require UPS and IPS measurements to determine the transport levels and TR-2PPE with a higher probe photon energy ($h\nu \geq 6$ eV) to identify both HOMO and LUMO states in the presence of an exciton; such data would allow to evaluate the exciton binding energy for this particular sample and to unambiguously determine the energy level alignment. However, provided that the exciton binding energies for the two molecular films are comparable, we can picture a scene analogous to the one reported by Tritsch et al.[10], in which electron transfer from the Tc $S_1$ to the CuPc LUMO is energetically favorable via an interfacial charge transfer (CT) state and occurs on the 400 fs time scale, while the slower triplet transfer through the interface is almost resonant but has a time constant of 45 ps.

Following the same procedure, we characterized the reversed interface. We first

grew a 2 - 3 ML CuPc film on the Ag(111) crystal and then deposited 1 - 2 ML Tc on top. With this deposition sequence, CuPc lies flat on the surface and Tc grows in a standing up orientation, as confirmed by polarization dependent NEXAFS (Figure A.3). UPS and TR-2PPE spectra for this system are shown in Figure 4.2a. For CuPc/Ag(111) the UPS spectrum shows a non-zero intensity at the Fermi edge that is associated with the CuPc LUMO that is partially filled in the molecular layer in contact with the substrate, due to charge transfer from it[21]. This complicates the TR-2PPE measurements on the CuPc film, as with the 4.8 eV probe photons we detect also direct photoemission from the LUMO, which prevents from properly identifying other peaks close to Fermi level. Moreover, at coverages higher than 3 ML, CuPc is known to grow in a Stransky-Krastanov morphology[38], thus keeping the signal contribution from the CuPc/Ag interface visible also for thicker films. To overcome this issue and define the energy levels of the molecular states in the CuPc/Ag interface, we investigated by means of TR-2PPE the well characterized CuPc/$C_{60}$/Ag(111) system. The presence of $C_{60}$ is known to favor an upright orientation of the phthalocyanine[39], but most importantly it shifts the CuPc $S_0$ to - 1.09 eV and its $S_1$ to 0.56 eV with respect to the Fermi level[40], thus separating it from the direct photoemission background. Assuming that the HOMO-LUMO gap is not affected by the different environments the CuPc molecules are surrounded by in the two configurations, we aligned the TR-2PPE spectra taken on the $C_{60}$ containing system to the kinetic energy scale of the CuPc/Ag(111) UPS spectrum by considering the different values of work function in the two cases, as measured by secondary electrons cutoff in UPS. As a result, we find $S_1$ at 0.1 eV and $T_1$ at - 0.7 eV. These values indicate an overlap of $S_1$ with the partially filled LUMO measured in UPS supposing that the exciton binding energy is sufficiently small in this system, which supports the assumptions made for this alignment. A scheme of the energy levels for the complete interface is reported in Figure 4.2c, which shows a notably different situation if compared to the previous sample. In particular, the Tc orbitals are shifted to lower ionization energies. Such behavior has been previously observed on interfaces of highly directional molecules, and was related to the molecular orientation: by calculating the charge distribution on the molecular crystals, it was shown that standing molecules present a lower ionization energy with respect to the lying down molecules[41], with a difference of 0.8 eV in pen-

tacene[24,42], and of 0.3 eV in CuPc[24]. This effect may explain the - 0.45 eV and + 0.14 eV variations in the ionization energies of Tc and CuPc HOMOs, respectively, in the two sample configurations and is also highlighting the importance of having a full control over the interface morphology for applicative purposes. A more complete picture of the potentials through the whole interface, accounting also for the bending of molecular orbitals using Oehzelt's model[22], would require a more accurate determination of the LUMO positions. This could be possible for instance by means of IPS and will be the target of future analyses on the system. Nevertheless, as we did for the previous sample, it is possible to qualitatively deduce the driving force for exciton transfer across the device. Here, excitons generated in Tc can separate at the interface with CuPc, as the electron transfer is energetically favored both from $S_1$ and $T_1$ states but there is a 0.2 eV barrier for hole transfer.

To summarize, for the CuPc/Tc/Ag(111) system we found an energy level alignment compatible with the transfer of excitons generated in Tc to CuPc, either from the $S_1$ or the $T_1$ state. In addition, transfer from Tc to the Ag substrate is also possible. On the inverted system, Tc/CuPc/Ag(111), electron transfer from Tc to CuPc is energetically favorable from both $S_1$ and $T_1$ states, with only the latter being beneficial for charge multiplication purposes. The negative carriers transferred to CuPc can eventually reach the substrate/electrode leaving an excess of positive charges available for collection in Tc.

### 4.1.2 Interpreting the core level shifts

Having characterized the frontier orbitals of the Tc/CuPc interface, we now possess a basic knowledge for interpreting the shifts that were detected on the core levels upon optical pumping. For the XPS analysis, the two interfaces were grown while monitoring the Ag3d and C1s photoemission lines. As an adequate signal from the Ag3d lines is needed to calibrate the binding energy scale in pump-probe measurements, this sets an upper limit for the film thickness to 3 - 4 nm. We roughly estimated the sample thickness by accounting for the Ag3d intensity attenuation in terms of the electron inelastic mean free path in solids[43]. For CuPc/Tc/Ag(111) this method is not highly accurate due to the Stranski-Krastanov morphology of the Tc multilayer[30,31], and yields 1.3 nm for Tc and

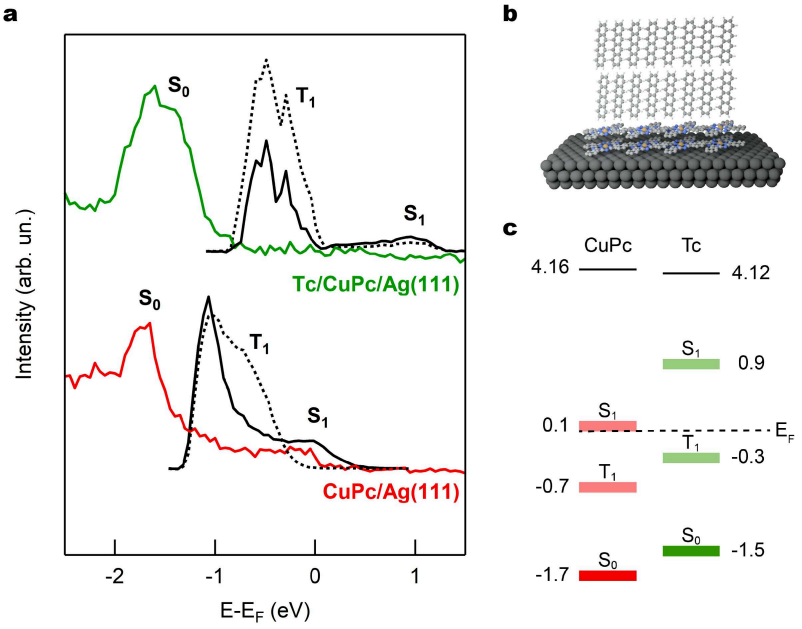


**Figure 4.2 | Energy levels of Tc/CuPc/Ag(111). a** UPS spectra for CuPc/Ag(111) (red) and for Tc/CuPc/Ag(111) (green). TR-2PPE spectra acquired around time zero (solid black lines) and at 5 ps delay (dashed black line) are overlaid to the photoemission spectra. To selectively excite Tc and CuPc, we used 515 and 626 nm pump photon energies, respectively. **b** Illustration of the interface morphology determined by polarization dependent NEXAFS. **c** Energy level alignment. Colored boxes represent the peak positions identified in panel **a**, black bars are the vacuum levels. All values are given in eV.

0.5 nm for the CuPc overlayer, which gives an average of 4 - 5 ML Tc (mostly flat) and 1 - 2 ML CuPc (slightly tilted). On the inverted interface, Tc/CuPc/Ag(111), we obtained 1.9 nm (6 - 7 ML) of flat lying CuPc and 1.7 nm (1 - 2 ML) of standing-up Tc on top. The C1s spectra for the two samples are shown in Figure 4.3. Notably, if we compare the spectra of the single Tc and CuPc films (dashed lines) to those of the whole interfaces (solid lines), we find binding energy shifts of the main peak that precisely reproduce the variations of the $S_0$ position reported in Figures 4.1c and 4.2c, therefore supporting the idea that such changes are related to the modification of the ionization potential due to the different molecular orientations[41].

In pump-probe photoemission measurements, we used 515 nm and 626 nm as pump wavelengths to selectively excite Tc and CuPc molecules, respectively, and

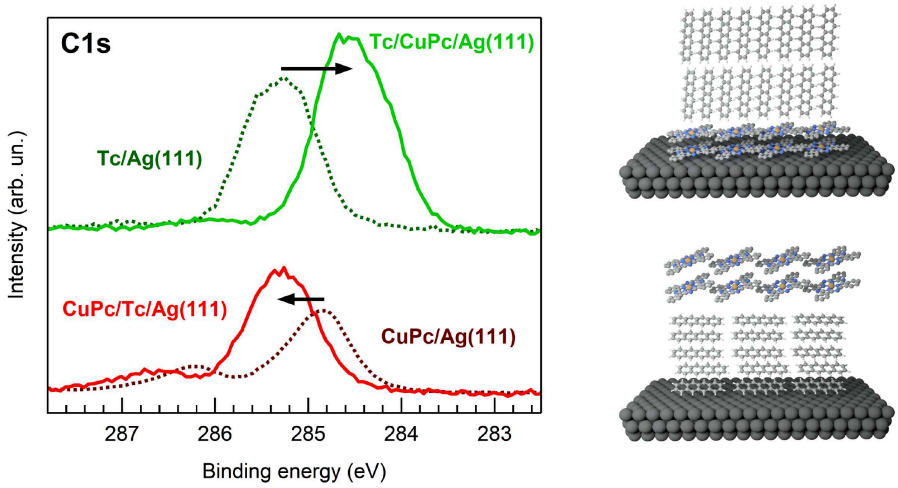


**Figure 4.3 | C1s photoemission for the two Tc/CuPc interfaces.** When Tc is grown on CuPc (solid green line), a 0.75 eV shift to lower binding energies is observed, if compared to Tc grown on the bare Ag(111) substrate (dashed green line). On the other hand CuPc shifts to higher binding energies (+ 0.4 eV) if grown on Tc (solid red line). Both shifts, pictured by the black arrows, are equivalent to the variations of the $S_0$ position that were previously observed for the two interfaces, which are related to different molecular orientations. XPS spectra were acquired with a photon energy of 515 eV.

515 eV as probe photon energy. For this analysis, we acquired the photoemission signal by integrating over the whole multibunch distribution instead of using only the hybrid bunches. The measured effects will therefore be mainly due to excited states with a lifetime at least comparable to the acquisition frame (1.5 µs). Before every measurement, a proper overlap between pump and probe pulses was ensured by detecting the space charge induced shifts on the $Ag3d_{5/2}$ line. In Figure 4.4 we show the C1s peak shift as a function of the pump fluence for the CuPc/Tc/Ag(111) interface. The peak positions were evaluated from the fits by accounting for a rigid shift of the C1s line, after aligning the $Ag3d_{5/2}$ peak to 368.3 eV for the whole dataset. All spectra were acquired in a laser on / laser off sequence, to ensure the reversibility of the effect and exclude radiation damage. Two significantly different behaviors are visible at different pump wavelengths: at 515 nm, for fluences higher than 0.5 µJ/cm$^2$, the shift to higher kinetic energies is almost constant ($\sim$ 0.08 eV), while at 626 nm it grows logarithmically with the fluence up to 0.3 eV. We speculate that such shifts are related

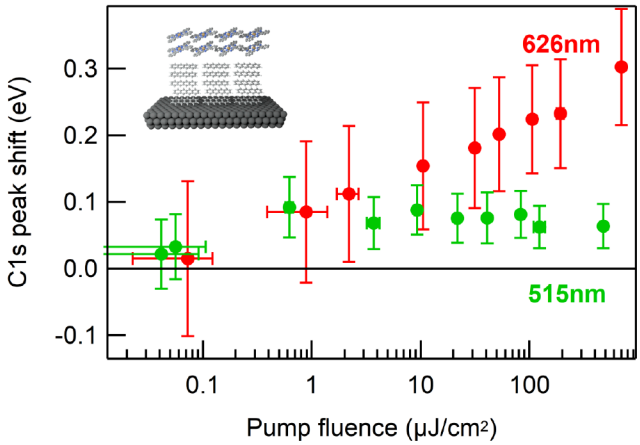


**Figure 4.4 | C1s peak shift as a function of pump fluence and wavelength for CuPc/Tc/Ag(111).** For 515 nm (green circles) and fluences higher than 0.5 uJ/cm$^2$ a constant shift of 0.08 eV to higher kinetic energies is detected. For 626 nm (red circles) the shift increases logarithmically with the pump fluence. In both cases, optical pumping results in a population of long lived excitons in CuPc, which generate a transient electric field that accelerates the photoemitted C1s electrons. Error bars represent one standard deviation.

to the exciton dissociation/transfer at the CuPc/Tc interface, as in the case of the pentacene/$C_{60}$ interface, which has been discussed in the previous chapter. Indeed, pump-probe photoemission performed on the single Tc and CuPc films on Ag(111) revealed negligible shifts (< 0.03 eV) with a 100 μJ/cm$^2$ fluence, supporting the hypothesis that the CuPc/Tc interface is playing a crucial role in the measurements that we are presenting.

By recalling the energy level alignments that we previously obtained, we can analyze the different scenarios that may explain the observed shifts. When pumping at 515 nm we are creating singlet excitons in Tc, which can either transfer to CuPc via a CT state or undergo fission and transfer resonantly as triplet excitons. The almost constant fluence dependence of the shift is explained by considering also the presencee of exciton-exciton annihilation: this competitive recombination process has been observed with fluences above 10 μJ/cm$^2$ in polycrystalline Tc films[44] and can have a lower threshold in our case, given the sample roughness that may confine the excitons in smaller volumes, increasing the probability of interactions. When pumping at 626 nm, instead, we are creating singlet exci-

tons in CuPc, which cannot transfer to Tc due to the unfavorable energy level alignment. As no saturation was found for the shift, we assume that the exciton-exciton annihilation threshold for CuPc is higher than 700 µJ/cm$^2$. In both cases, the result of optical pumping is a transient electric field due to a population of long lived (> 1.5 µs) excitons, i.e. triplets, in the CuPc film, which results in the shift of the C1s peak to higher kinetic energies. As already mentioned for the pentacene/$C_{60}$ measurements, a complete model to describe the observed effects should consider also the dielectric response of the whole environment to the presence of the excitons[45], therefore, once again, micro-electrostatic simulations would be beneficial.

In Figure 4.5 we show the fluence dependence of the C1s peak shift for the inverted interface, Tc/CuPc/Ag(111). With the 626 nm pump, the measured shift is compatible to zero at any fluence; as the transfer to Tc is not energetically favored, excitons generated in CuPc can only diffuse to the Ag substrate, and do not generate any transient field to perturb the photoemitted electrons, at least on the microsecond time scale. On the other hand, excitons created on Tc by pumping at 515 nm can dissociate at the interface with CuPc either from $S_1$ or $T_1$ states (reasonably through CT intermediates[46]); after the dissociation, the

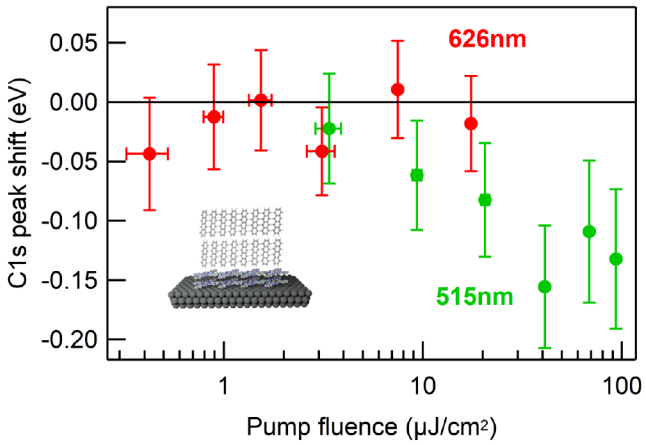


**Figure 4.5 | C1s peak shift as a function of pump fluence and wavelength for Tc/CuPc/Ag(111).** With a 626 nm pump (red circles) the peak shift is compatible to zero, while pumping at 515 nm (green circles) leads to a shift towards lower kinetic energies. The latter may be explained by the exciton dissociation at the Tc/CuPc interface, leaving an excess of positive charges in the Tc layer.

electrons can travel through CuPc to reach the substrate, while the holes remain in the Tc layer leaving an excess of positive charges. We speculate that a lifetime long enough of these holes could explain the shift to lower kinetic energies based on simple electrostatic considerations.

## 4.2 Final remarks

I have reported here the characterization of the Tc/CuPc interface performed at the ANCHOR-SUNDYN endstation, in which UPS, TR-2PPE and pump-probe XPS were combined with the aim of describing the exciton transfer through the interface. We used UPS and TR-2PPE to determine the energy level alignment of the interface, which was seen to depend on the deposition sequence of the two organic films or, better, on the mutual orientation of the two molecular species. A similar effect was observed also on the C1s photoemission peak, and we assigned it to the variation of the ionization energy due to different molecular orientations. The attempt of obtaining the energy level alignment from UPS and TR-2PPE, however, also revealed the necessity of determining the exciton binding energies in order to clearly distinguish between optical and transport levels for the organic semiconductor; to this aim, additional IPS measurements would complete the picture. Still, by assuming a comparable exciton binding energy in the two materials, we interpreted the core level shifts measured in pump-probe XPS as a consequence of the exciton dynamics driven by the tentative energy level alignment. As the shifts that we observed appeared to be rigid shifts of the C1s peaks, we can confidently claim that they are due to the presence of a transient electric field or to a global modification of the ionization energy rather than to a local effect, since in the latter case we would expect a broadening of the C1s line, with only the small percentage of excited molecules shifting with respect to the unperturbed ones. A complete modeling of such electric field must include not only the presence of charge carriers, but also the dielectric response of the whole interface. We expect that the calculations which will be performed for the analogous case of pentacene/$C_{60}$ will prove to be useful for the understanding of the dynamics in the Tc/CuPc interface as well.
To conclude, we have shown that pump-probe XPS can be used as a tool for investigating the rise of transient electric fields related to the exciton dynamics in or-

ganic heterojunctions. Moreover, by tuning the wavelength of the optical pump to the absorption maxima of Tc and CuPc, we were able to examine the different scenarios that follow the photoexcitation of either one or the other material: our results seem to suggest that charge transfer can occur from Tc to CuPc. Since the measurements were performed using the multibunch photons as a probe, the effects that we observed are averaged over a time scale of 1.5 µs and therefore we deem them linked entirely to the long-lived triplet excitons.

# References


1. Jadhav, P. J.; Mohanty, A.; Sussman, J.; Lee, J.; Baldo, M. A. Singlet Exciton Fission in Nanostructured Organic Solar Cells. *Nano Letters* **2011**, *11*, 1495–1498.

2. Congreve, D. N.; Lee, J.; Thompson, N. J.; Hontz, E.; Yost, S. R.; Reusswig, P. D.; Bahlke, M. E.; Reineke, S.; Van Voorhis, T.; Baldo, M. A. External Quantum Efficiency Above 100% in a Singlet-Exciton-Fission-Based Organic Photovoltaic Cell. *Science* **2013**, *340*, 334–337.

3. Thompson, N. J.; Congreve, D. N.; Goldberg, D.; Menon, V. M.; Baldo, M. A. Slow light enhanced singlet exciton fission solar cells with a 126% yield of electrons per photon. *Applied Physics Letters* **2013**, *103*, 1–4.

4. Thompson, N. J.; Wilson, M. W. B.; Congreve, D. N.; Brown, P. R.; Scherer, J. M.; Bischof, T. S.; Wu, M.; Geva, N.; Welborn, M.; Voorhis, T. V.; Bulović, V.; Bawendi, M. G.; Baldo, M. A. Energy harvesting of non-emissive triplet excitons in tetracene by emissive PbS nanocrystals. *Nature Materials* **2014**, *13*, 1039–1043.

5. Einzinger, M.; Wu, T.; Kompalla, J. F.; Smith, H. L.; Perkinson, C. F.; Nienhaus, L.; Wieghold, S.; Congreve, D. N.; Kahn, A.; Bawendi, M. G.; Baldo, M. A. Sensitization of silicon by singlet exciton fission in tetracene. *Nature* **2019**, *571*, 90–94.

6. Brabec, C. J.; Cravino, A.; Meissner, D.; Sariciftci, N. S.; Fromherz, T.; Rispens, M. T.; Sanchez, L.; Hummelen, J. C. Origin of the Open Circuit Voltage of Plastic Solar Cells. *Advanced Functional Materials* **2001**, *11*, 374–380.

7. Vandewal, K.; Gadisa, A.; Oosterbaan, W. D.; Bertho, S.; Banishoeib, F.; Van Severen, I.; Lutsen, L.; Cleij, T. J.; Vanderzande, D.; Manca, J. V. The Relation Between Open-Circuit Voltage and the Onset of Photocurrent Generation by Charge-Transfer Absorption in Polymer:Fullerene Bulk Heterojunction Solar Cells. *Advanced Functional Materials* **2008**, *18*, 2064–2070.

8. Shockley, W.; Queisser, H. J. Detailed balance limit of efficiency of p-n junction solar cells. *Journal of Applied Physics* **1961**, *32*, 510–519.

9. Lee, J.; Jadhav, P.; Reusswig, P. D.; Yost, S. R.; Thompson, N. J.; Congreve, D. N.; Hontz, E.; Van Voorhis, T.; Baldo, M. A. Singlet exciton fission photovoltaics. *Accounts of Chemical Research* **2013**, *46*, 1300–1311.

10. Tritsch, J. R.; Chan, W.-L.; Wu, X.; Monahan, N. R.; Zhu, X.-Y. Harvesting singlet fission for solar energy conversion via triplet energy transfer. *Nature Communications* **2013**, *4*, 1–7.

11. MacQueen, R. W.; Liebhaber, M.; Niederhausen, J.; Mews, M.; Gersmann, C.; Jäckle, S.; Jäger, K.; Tayebjee, M. J. Y.; Schmidt, T. W.; Rech, B.; Lips, K. Crystalline silicon solar cells with tetracene interlayers: the path to silicon-singlet fission heterojunction devices. *Materials Horizons* **2018**, *5*, 1065–1075.

12. Wilson, M. W. B.; Rao, A.; Johnson, K.; Gélinas, S.; di Pietro, R.; Clark, J.; Friend, R. H. Temperature-Independent Singlet Exciton Fission in Tetracene. *Journal of the American Chemical Society* **2013**, *135*, 16680–16688.

13. Chan, W.-L.; Ligges, M.; Zhu, X.-Y. The energy barrier in singlet fission can be overcome through coherent coupling and entropic gain. *Nature Chemistry* **2012**, *4*, 840–845.

14. Burdett, J. J.; Gosztola, D.; Bardeen, C. J. The dependence of singlet exciton relaxation on excitation density and temperature in polycrystalline tetracene thin films: Kinetic evidence for a dark intermediate state and implications for singlet fission. *Journal of Chemical Physics* **2011**, *135*.

15. Wan, Y.; Guo, Z.; Zhu, T.; Yan, S.; Johnson, J.; Huang, L. Cooperative singlet and triplet exciton transport in tetracene crystals visualized by ultrafast microscopy. *Nature Chemistry* **2015**, *7*, 785–792.

16. Zhu, T.; Wan, Y.; Guo, Z.; Johnson, J.; Huang, L. Two Birds with One Stone: Tailoring Singlet Fission for Both Triplet Yield and Exciton Diffusion Length. *Advanced Materials* **2016**, *28*, 7539–7547.

17. Zhu, T.; Huang, L. Exciton Transport in Singlet Fission Materials: A New Hare and Tortoise Story. *The Journal of Physical Chemistry Letters* **2018**, *9*, 6502–6510.

18. Zhu, X. Y. How to draw energy level diagrams in excitonic solar cells. *Journal of Physical Chemistry Letters* **2014**, *5*, 2283–2288.

19. Li, Y.; Li, P.; Lu, Z. H. Mapping Energy Levels for Organic Heterojunctions. *Advanced Materials* **2017**, *29*, 1–7.

20. Bao, Q.; Braun, S.; Wang, C.; Liu, X.; Fahlman, M. Interfaces of (Ultra)thin Polymer Films in Organic Electronics. *Advanced Materials Interfaces* **2019**, *6*, 1–15.

21. Stadtmüller, B.; Lüftner, D.; Willenbockel, M.; Reinisch, E. M.; Sueyoshi, T.; Koller, G.; Soubatch, S.; Ramsey, M. G.; Puschnig, P.; Tautz, F. S.; Kumpf, C. Unexpected interplay of bonding height and energy level alignment at heteromolecular hybrid interfaces. *Nature Communications* **2014**, *5*, 3685.

22. Oehzelt, M.; Akaike, K.; Koch, N.; Heimel, G. Energy-level alignment at organic heterointerfaces. *Science Advances* **2015**, *1*, e1501127.

23. Osikowicz, W.; de Jong, M. P.; Salaneck, W. R. Formation of the Interfacial Dipole at Organic-Organic Interfaces: $C_{60}$/Polymer Interfaces. *Advanced Materials* **2007**, *19*, 4213–4217.

24. Li, Y.; Li, P.; Lu, Z.-h. Molecular Orientation and Energy Levels at Organic Interfaces. *Advanced Electronic Materials* **2016**, *2*, 1600306.

25. Waas, D.; Rückerl, F.; Knupfer, M.; Büchner, B. Energy-level alignment at interfaces between manganese phthalocyanine and $C_{60}$. *Beilstein Journal of Nanotechnology* **2017**, *8*, 927–932.

26. Tang, J. X.; Lee, C. S.; Lee, S. T. Electronic structures of organic/organic heterojunctions: From vacuum level alignment to Fermi level pinning. *Journal of Applied Physics* **2007**, *101*, 064504.

27. Zhao, W.; Salomon, E.; Zhang, Q.; Barlow, S.; Marder, S. R.; Kahn, A. Substrate-dependent electronic structure of an organic heterojunction. *Physical Review B* **2008**, *77*, 165336.

28. Sai, N.; Gearba, R.; Dolocan, A.; R. Tritsch, J.; Chan, W.-L.; R. Chelikowsky, J.; Leung, K.; Zhu, X. Understanding the Interface Dipole of Copper Phthalocyanine (CuPc)/$C_{60}$: Theory and Experiment. *The Journal of Physical Chemistry Letters* **2012**, *3*, 2173–2177.

29. Soubatch, S.; Kröger, I.; Kumpf, C.; Tautz, F. S. Structure and growth of tetracene on Ag(111). *Physical Review B* **2011**, *84*, 195440.

30. Langner, A.; Hauschild, A.; Fahrenholz, S.; Sokolowski, M. Structural properties of tetracene films on Ag(1 1 1) investigated by SPA-LEED and TPD. *Surface Science* **2005**, *574*, 153–165.

31. Gonella, G.; Dai, H.-L.; J. Rockey, T. Tetracene Monolayer and Multilayer Thin Films on Ag(111): Substrate-Adsorbate Charge-Transfer Bonding and Inter-Adsorbate Interaction. *The Journal of Physical Chemistry C* **2008**, *112*, 4696–4703.

32. Krause, S.; Casu, M. B.; Schöll, A.; Umbach, E. Determination of transport levels of organic semiconductors by UPS and IPS. *New Journal of Physics* **2008**, *10*, 085001.

33. Conwell, E. Definition of exciton binding energy for conducting polymers. *Synthetic Metals* **1996**, *83*, 101–102.

34. Campbell, I. H.; Hagler, T. W.; Smith, D. L.; Ferraris, J. P. Direct measurement of conjugated polymer electronic excitation energies using metal/polymer/metal structures. *Physical Review Letters* **1996**, *76*, 1900–1903.

35. Hill, I.; Kahn, A.; Soos, Z.; Pascal, Jr, R. Charge-separation energy in films of $\pi$-conjugated organic molecules. *Chemical Physics Letters* **2000**, *327*, 181–188.

36. Nayak, P. K. Exciton binding energy in small organic conjugated molecule. *Synthetic Metals* **2013**, *174*, 42–45.

37. Knupfer, M. Exciton binding energies in organic semiconductors. *Applied Physics A* **2003**, *77*, 623–626.

38. Thussing, S.; Jakob, P. Structural and Vibrational Properties of CuPc/Ag(111) Ultrathin Films. *The Journal of Physical Chemistry C* **2016**, *120*, 9904–9913.

39. Huang, H.; Chen, W.; Chen, S.; Qi, D. C.; Gao, X. Y.; Wee, A. T. S. Molecular orientation of CuPc thin films on $C_{60}$/Ag (111). *Applied Physics Letters* **2009**, *94*, 92–95.

40. Dutton, G. J.; Jin, W.; Reutt-Robey, J. E.; Robey, S. W. Ultrafast charge-transfer processes at an oriented phthalocyanine/$C_{60}$ interface. *Physical Review B* **2010**, *82*, 073407.

41. Duhm, S.; Heimel, G.; Salzmann, I.; Glowatzki, H.; Johnson, R. L.; Vollmer, A.; Rabe, J. P.; Koch, N. Orientation-dependent ionization energies and interface dipoles in ordered molecular assemblies. *Nature Materials* **2008**, *7*, 326–332.

42. Heimel, G.; Koch, N. *Interface Controlled Organic Thin Films*; 2009; Vol. 129; pp 141–145.

43. Cumpson, P. J.; Seah, M. P. Elastic Scattering Corrections in AES and XPS. II. Estimating Attenuation Lengths and Conditions Required for their Valid Use in Overlayer/Substrate Experiments. *Surface and Interface Analysis* **1997**, *25*, 430–446.

44. Burdett, J. J.; Müller, A. M.; Gosztola, D.; Bardeen, C. J. Excited state dynamics in solid and monomeric tetracene: The roles of superradiance and exciton fission. *The Journal of Chemical Physics* **2010**, *133*, 144506.

45. Stadtmüller, B.; Emmerich, S.; Jungkenn, D.; Haag, N.; Rollinger, M.; Eich, S.; Maniraj, M.; Aeschlimann, M.; Cinchetti, M.; Mathias, S. Strong modification of the transport level alignment in organic materials after optical excitation. *Nature Communications* **2019**, *10*, 1470.

46. Deibel, C.; Strobel, T.; Dyakonov, V. Role of the Charge Transfer State in Organic Donor-Acceptor Solar Cells. *Advanced Materials* **2010**, *22*, 4097–4111.

# 5 Conclusions

I have reported the technical development of the ANCHOR-SUNDYN endstation: With the current setup, XPS and XAS spectroscopies can be measured in a pump-probe fashion by exciting the sample with a tunable optical laser, which is also used to perform time-resolved 2PPE. The combination of these techniques allows tracking the exciton dynamics in organic films from the 0.3 - 250 ps time scale covered by TR-2PPE, to the 0.1 - 100 ns range that is accessible with time-resolved X-ray spectroscopies. Time-resolved techniques at the ANCHOR-SUNDYN endstation are also combined with conventional UV and X-ray spectroscopies, which are routinely used for the *in situ* characterization of organic films.

We studied in detail the pentacene/$C_{60}$ system and, for the first time, we detected the triplet excited state fingerprint in TR-XAS spectra, which was observed with a $0.3 \pm 0.2$ ns lifetime. Faster dynamics have been explored at the FLASH FEL by means of TR-XPS, which revealed spectral shifts peaked at 6 ps after the optical excitation; we assigned such effects to transient electric fields generated at the pentacene/$C_{60}$ interface after triplet exciton dissociation, based on the close correspondence between the time scale of the latter process and the delay in the photoelectron response. At our beamline, we observed analogous effects on tetracene/CuPc interfaces in the microsecond time scale; by tuning the pump wavelength we discriminated the behavior of excitons created on the two sides of the organic interface, and we concluded that charge transfer occurs from tetracene to CuPc. Our description is supported by the favorable energy level alignment in the heterojunction, which was determined by combining UPS and 2PPE spectra and is in agreement with previous studies. Moreover, on the tetracene/CuPc system, we have shown how the molecular orientation influ-

ences the ionization energy of valence (and core) states. Such effect underlines the importance of controlling the film morphology in the design of complex architectures, as it actively influences the electronic properties of the interface. To this extent, the versatility of the ANCHOR-SUNDYN endstation is a significant advantage, as it allows to complement time-resolved measurements with static XPS, NEXAFS and ARPES spectroscopies for correlating the observed dynamics to the structural and electronic properties of the sample.

The time-resolved XPS data shown for pentacene/$C_{60}$ and tetracene/CuPc seem to suggest that a spectroscopic evidence for charge transfer across organic interfaces may be found in the kinetic energy shift of the core photoelectrons, which are accelerated (or decelerated) by the transient electric fields that arise after exciton dissociation. In contrast to the more widely used TR-2PPE spectroscopies, TR-XPS can be used to obtain site specific information that is useful when studying complex heterostructures. Nevertheless, due to the experimental requirements, this technique is currently performed in a limited number of facilities worldwide. In particular, pulsed X-ray radiation is available at synchrotrons, FELs and HHG setups but, in terms of count rate and probe space charge effects, the best experimental conditions are found at synchrotron facilities, which routinely supply tunable, high repetition rate X-ray beams. In comparison to FELs and HHGs, however, the synchrotron pulse width is 2 - 3 orders of magnitude larger, thus affecting the temporal resolution, which in our setup limits the observable dynamics to time scales in the order of 100 ps or slower.

As I have shown in my thesis, the current resolution is sufficient for the characterization of triplet excited states in singlet fission chromophores, but planned developments of the Elettra storage ring are expected to push the X-ray pulse width down to the picosecond range, therefore allowing us to access also the 1 - 10 ps charge transfer processes that we identified in our measurements at the FLASH FEL. Along with experimental advancements, it is also essential to develop a theoretical approach for accurately modeling the transient fields resulting from exciton dissociation, by taking into account both the presence of charge carriers and the dielectric response of the molecular environment. In an attempt to perform a quantitative analysis of the TR-XPS data obtained on the pentacene/$C_{60}$ interface, we asked for micro-electrostatic simulations of the triplet transfer process for such system, which, if successful, may be repeated for the tetracene/CuPc

dataset.

Apart from experimental and theoretical progress, there are still a couple of open questions that we aim to answer for the tetracene/CuPc system: the first one is concerning the exciton binding energies in the two chromophores, which have to be determined to provide a more accurate energy level alignment at the interface; the second one is related to the not yet measured time scale of the photoelectron response. The TR-XPS spectra presented in this thesis were acquired using the multibunch operation of Elettra, therefore the effect we have seen is averaged over the whole acquisition window (1.5 μs). It would be interesting to measure the photoelectron shift using the hybrid bunch as a probe, in order to evaluate the decay time of the dynamics in this interface. Eventually, it will also be fundamental to step away from polyacene chromophores and focus on the characterization of more stable compounds, e.g. perylene derivatives, which are more suitable for future technological applications.

# A Molecular orientation in Tc/CuPc interfaces

To qualitatively determine the molecular orientation of Tc and CuPc for the two deposition sequences we performed polarization dependent NEXAFS. S-polarized spectra (blue traces) are acquired at normal incidence, while p-polarized spectra (red traces) are measured at grazing incidence (i.e. 5° with respect to the sample surface). Figure A.1a shows the carbon K-edge absorption for a 4 - 5 ML

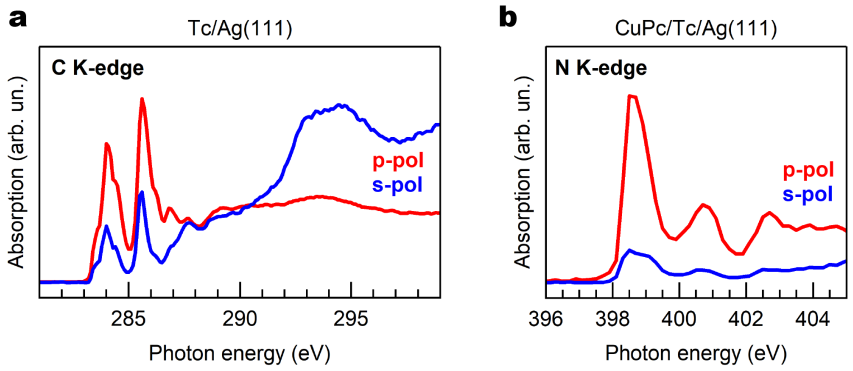


**Figure A.1 | Polarization dependent NEXAFS for CuPc/Tc/Ag(111). a** C K-edge spectra for Tc/Ag(111). The film is not fully oriented, and the dichroism is compatible to the $\beta$-phase, which presents an average tilt of $\sim 35°$. **b** N K-edge spectra for CuPc/Tc/Ag(111). The dichroism is not total, indicating that CuPc molecules grown on Tc are slightly tilted.

Tc film on Ag(111). In the literature, when grown on Ag(111) at 230 K, Tc is known to form a flat α-phase monolayer [1], while higher coverages form Stranski–Krastanov structures [2,3]. The slight dichroism in our spectra is comparable to the data reported for the bilayer β-phase [4], with the molecules presenting an average

tilt of ~35° from the substrate plane. The roughness of Tc is also resulting in a slightly tilted orientation of the CuPc molecules that are deposited on top of it, as emerges from the nitrogen K-edge spectra shown in Figure A.1b.

On the other hand, by reversing the deposition sequence, CuPc molecules are

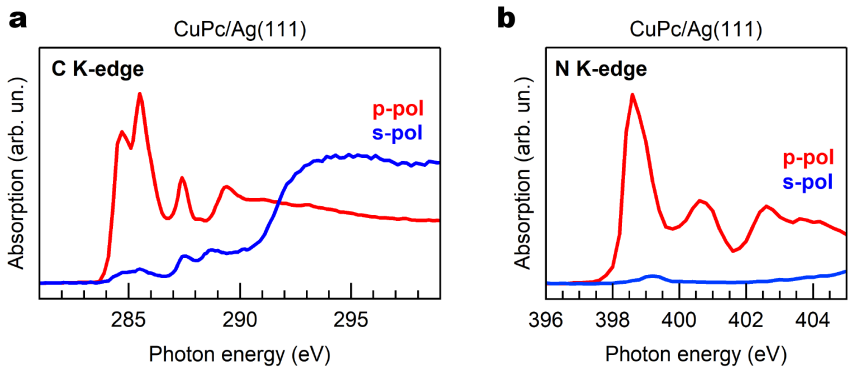


**Figure A.2 | Polarization dependent NEXAFS for CuPc/Ag(111). a** C K-edge and **b** N K-edge spectra for CuPc/Ag(111). The dichroism is stronger if compared to CuPc deposited on top of Tc, meaning that the film is better ordered with the molecules lying flat on the surface.

lying flat on the Ag(111) surface, as evidenced by the almost perfect dichroism in both carbon and nitrogen K-edges (Figure A.2). When depositing Tc on top

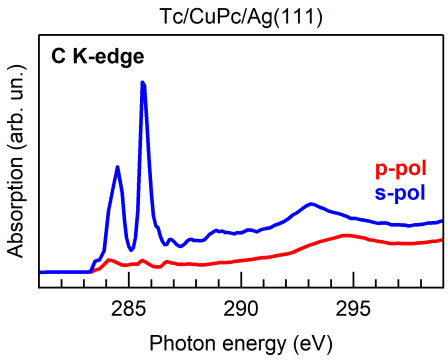


**Figure A.3 | Polarization dependent NEXAFS for Tc/CuPc/Ag(111).** The dichroism is inverted with respect to the spectra acquired on Tc/Ag(111): Tc grows in an upright orientation if deposited on CuPc.

(Figure A.3), the dichroism on the carbon K-edge is reversed; due to a lower interaction with the substrate, Tc molecules grow in an upright orientation. An

analogous behavior has been observed when depositing pentacene on a CuPc monolayer[5]. We acknowledge a modification of the shape of the LUMO resonance with respect to the one observed on the Tc/Ag(111) sample, which cannot be explained as the mere contribution of CuPc to the absorption signal, and has to be furtherly investigated.

# References


1. Soubatch, S.; Kröger, I.; Kumpf, C.; Tautz, F. S. Structure and growth of tetracene on Ag(111). *Physical Review B* **2011**, *84*, 195440.

2. Langner, A.; Hauschild, A.; Fahrenholz, S.; Sokolowski, M. Structural properties of tetracene films on Ag(1 1 1) investigated by SPA-LEED and TPD. *Surface Science* **2005**, *574*, 153–165.

3. Gonella, G.; Dai, H.-L.; J. Rockey, T. Tetracene Monolayer and Multilayer Thin Films on Ag(111): Substrate-Adsorbate Charge-Transfer Bonding and Inter-Adsorbate Interaction. *The Journal of Physical Chemistry C* **2008**, *112*, 4696–4703.

4. Sueyoshi, T.; Willenbockel, M.; Naboka, M.; Nefedov, A.; Soubatch, S.; Wöll, C.; Tautz, F. S. Spontaneous Change in Molecular Orientation at Order–Disorder Transition of Tetracene on Ag(111). *The Journal of Physical Chemistry C* **2013**, *117*, 9212–9222.

5. Mänz, A.; Hauke, A. A.; Witte, G. Copper Phthalocyanine as Contact Layers for Pentacene Films Grown on Coinage Metals. *The Journal of Physical Chemistry C* **2018**, *122*, 2165–2172.

# B List of Acronyms

| | |
|---|---|
| **2PPE** | Two-Photon Photoemission |
| **3HC** | Third Harmonic Cavity |
| **AEY** | Auger Electron Yield |
| **ARPES** | Angle Resolved Photoemission Spectroscopy |
| **BBO** | Beta Barium Borate |
| **BF** | Bunch Filling |
| **ES** | Exit Slits |
| **FEL** | Free Electron Laser |
| **FWHM** | Full Width at Half Maximum |
| **HB** | Hybrid Bunch |
| **HHG** | High Harmonic Generation |
| **IPS** | Inverse Photoemission |
| **IR** | Infrared |
| **MB** | Multibunch |
| **ML** | Monolayer |
| **NEXAFS** | Near Edge X-ray Absorption Fine Structure |
| **OPA** | Optical Parametric Amplifier |

| | |
|---|---|
| **PVD** | Physical Vapor Deposition |
| **RF** | Radio Frequency |
| **RP** | Resolving Power |
| **PMPG** | Plane Mirror Plane Grating |
| **SASE** | Self-Amplified Spontaneous Emission |
| **SB** | Single Bunch |
| **TA** | Transient Absorption |
| **TDDFT** | Time-Dependent Density Functional Theory |
| **ToF** | Time of Flight |
| **TR-2PPE** | Time-Resolved Two-Photon Photoemission |
| **TR-ARPES** | Time- and Angle-Resolved Photoemission Spectroscopy |
| **TR-XAS** | Time-Resolved X-ray Absorption Spectroscopy |
| **TR-XPS** | Time-Resolved X-ray Photoemission Spectroscopy |
| **UHV** | Ultra-High Vacuum |
| **UPS** | Ultraviolet Photoelectron Spectroscopy |
| **UV** | Ultraviolet |
| **XAS** | X-ray Absorption Spectroscopy |
| **XPS** | X-ray Photoelectron Spectroscopy |
| **YAG** | Yttrium Aluminum Garnet |

# Ringraziamenti

Tre anni di dottorato sono (quasi) volati, ed è ora di spendere qualche parola per ringraziare tutti quelli che hanno contribuito in questo mio percorso.
I primi due nomi in questa lista sono stati equamente fondamentali per la mia crescita, da quando sono arrivato ad ALOISA come laureando fino ad ora, e devo ringraziare entrambi per le numerose e indispensabili discussioni sull'interpretazione delle misure di questa tesi.
In ordine prettamente alfabetico: Albano, o forse sarebbe meglio dire professor Cossaro, grazie per il costante supporto e per avermi insegnato tutto quel poco che sono riuscito ad imparare in questi anni; Martina, grazie per le giornate passate a cercare il tempo zero fra i vari capricci di Tangerina e a misurare tutte le combinazioni possibili di pentacene e tetracene quando finalmente il laser ha iniziato a collaborare.
Grazie al Morgante e alle sue provvidenziali incursioni in laboratorio alle 18, sempre con nuovi spunti per migliorare i nostri esperimenti, e al resto del team ALOISA: Luca e Alberto, pronti a risolvere qualsiasi dubbio (scientifico e non).
E un grazie anche a Matus, con cui ho condiviso gran parte di questi tre anni a stringere flange.
Stefano De Toffol, non mi stancherò mai di sottolineare il grande impatto che tu hai avuto come insegnante al liceo, senza la passione che tu sei riuscito a trasmettermi per la fisica probabilmente le mie scelte sarebbero state diverse.
E per finire grazie a mamma e papà che mi hanno sempre sostenuto in questi anni di università e a nonna Angelina, che spero sia finalmente contenta che io sia diventato un dottore di ricerca.